aerospace

MDPI

Article

Transferability-Guided Residual Attention Domain Adaptation for Unsupervised Cross-Condition Aero-Engine Gas-Path Fault Diagnosis

Haobin Xu [1], Kailong Cai [2] and Lishun Chen [1,*]

[1] School of Civil Aviation and Transportation, Nanchang Hangkong University, Nanchang 330063, China; xuhaobin0012@163.com
[2] School of Aerospace Engineering, Nanchang Institute of Technology, Nanchang 330044, China; caikailong@sina.com
* Correspondence: chenlishun2026@163.com; Tel.: +86-13732978276

Abstract

Cross-condition aero-engine gas-path fault diagnosis remains challenging because gas-path parameters exhibit heterogeneous transferability, hidden feature distributions shift substantially across operating conditions, and the class structure of the unlabeled target domain is often unstable. To address these issues, this study proposes a Transferability-Guided Residual Attention Domain Adaptation Network (TG-RADAN) for unsupervised cross-condition aero-engine gas-path fault diagnosis. First, a Transferability Index (TI) is constructed by jointly considering source-domain fault discriminability and cross-domain distribution stability. Based on the TI, a learnable feature-gating mechanism is introduced to adaptively reweight gas-path parameters and suppress operating-condition-sensitive features. Second, a residual-attention encoder with domain-specific batch normalization is developed to enhance fault-discriminative representations while mitigating hidden-layer statistical discrepancies between domains. Third, conditional adversarial domain adaptation, high-confidence pseudo-label prototype alignment, and target entropy minimization are jointly employed to improve class-conditional alignment and preserve the target-domain structure. Experiments on 12 cross-condition transfer tasks demonstrate that TG-RADAN achieves average accuracies of 94.43% and 94.41% on the two groups of transfer tasks, respectively, outperforming the conventional CDAN baseline by 11.94% and 12.91%. Ablation results show that the complete model improves upon the model without TI-guided gating by 2.69% and 3.20%, respectively. These findings indicate that TG-RADAN can effectively improve the transferability, robustness, and interpretability of unsupervised cross-condition aero-engine gas-path fault diagnosis.

Keywords: aero-engine; gas-path fault diagnosis; cross-condition diagnosis; unsupervised domain adaptation; transferability index; learnable gating

Check for updates

Received: 17 July 2026
Revised: 22 August 2026
Accepted: 27 August 2026
Published: 28 August 2026

Copyright: © 2026 by the authors. Licensee MDPI, Basel, Switzerland. This article is an open access article distributed under the terms and conditions of the Creative Commons Attribution (CC BY) license.

1. Introduction

As the core power source of an aircraft, the aero-engine is an integrated system involving complex aerodynamic and thermodynamic processes, and its operating condition is directly related to flight safety. Owing to long-term operation under harsh conditions such as high temperature, high pressure, and heavy load, gas-path components are prone to performance degradation and faults. Therefore, accurate and reliable gas-path fault diagnosis is of great importance for ensuring the safe operation of aero-engines [1]. With the

rapid development of digital and intelligent technologies, data-driven intelligent diagnosis methods have become an active research topic. Compared with traditional approaches that rely heavily on physical mechanism analysis and expert experience, data-driven methods can automatically extract fault-related information from complex monitoring signals, thereby offering clear advantages in improving diagnostic efficiency [2,3].

In recent years, deep learning methods have achieved promising performance in aero-engine fault diagnosis owing to their strong nonlinear modeling and representation learning capabilities. Meanwhile, intelligent diagnosis algorithms, such as extreme learning machine (ELM), support vector machine (SVM), and back-propagation neural network (BPNN), can learn relatively stable fault representations and achieve high recognition accuracy when the training and testing data are collected under the same operating condition or follow the same distribution [4,5]. However, in practical engineering scenarios, labeled aero-engine data are often difficult to obtain, and the health states of newly collected data are usually unknown. Moreover, monitoring data may be acquired under different flight altitudes and Mach numbers, leading to substantial distribution discrepancies across operating conditions. As a result, conventional supervised learning models are prone to feature mismatch and performance degradation in cross-condition diagnosis tasks, which significantly limits their generalization capability [6,7].

Unsupervised domain adaptation (UDA) provides a promising solution for cross-condition aero-engine fault diagnosis. By leveraging labeled source-domain data and unlabeled target-domain data, domain adaptation methods aim to reduce the distribution discrepancy between the source and target domains in a shared feature space, thereby enabling effective knowledge transfer [8]. Among existing methods, distribution-metric-based transfer diagnosis approaches improve cross-domain consistency by imposing statistical distance constraints between different domains, whereas adversarial-learning-based methods encourage the feature extractor to learn domain-invariant representations through a domain discriminator [9,10]. For example, Han et al. [11] proposed a joint-distribution adaptation deep transfer network, in which a deep neural network was combined with maximum mean discrepancy (MMD) to simultaneously align the marginal and conditional distributions of the source and target domains, thereby providing an end-to-end transfer framework for industrial intelligent fault diagnosis. Shao et al. [12] adopted a deep convolutional network pretraining and parameter fine-tuning strategy, and achieved high-accuracy fault diagnosis for rotating machinery and related equipment through deep transfer learning, which significantly improved generalization performance under small-sample conditions. Guo et al. [13] designed a deep convolutional transfer network that integrates one-dimensional convolutional feature extraction, distribution adaptation, and domain-adversarial training to realize cross-device fault recognition with unlabeled target-domain data. Sun et al. [14] combined sparse autoencoders with deep transfer learning and performed remaining useful life prediction of manufacturing tools through feature transfer and distribution alignment, effectively addressing operating-condition discrepancies and data scarcity. Qiao et al. [15] constructed an adaptive weighted multi-scale convolutional neural network, in which multi-scale convolutions were used to automatically extract fault features from different frequency bands and assign adaptive weights, thereby substantially improving diagnostic accuracy and stability under complex conditions such as variable speeds and loads. Although these methods have made considerable progress, several key challenges remain in cross-condition fault diagnosis of aero-engines.

First, gas-path parameters exhibit pronounced physical heterogeneity, and different measured variables show unequal sensitivities to fault degradation and operating-condition disturbances [16]. Some parameters possess strong fault-discriminative capability while remaining relatively stable across operating conditions, whereas others exhibit larger

distribution variations with changes in altitude and Mach number and may introduce stronger condition-specific discrepancies during cross-condition transfer [17]. However, most existing domain adaptation methods implicitly assume that all input features have comparable transferability and perform uniform alignment in the overall feature space. As a result, operating-condition-sensitive features may be incorrectly incorporated into transferable representations, leading to negative transfer. Second, variations in operating conditions not only affect the distribution of raw gas-path parameters but also further alter the statistical properties of hidden representations in deep networks. Existing deep domain adaptation models usually rely on shared feature encoding and unified normalization statistics, making it difficult to distinguish differences in the means and variances of hidden activations under different operating conditions. When significant statistical discrepancies exist between the source and target domains, shared normalization may bias the learned representations toward the source domain and weaken the stability of feature learning in the target domain. Finally, adversarial distribution alignment alone cannot sufficiently guarantee a well-structured target-domain class distribution. In the unsupervised target domain, the absence of ground-truth label constraints may cause target samples to be distributed near decision boundaries. This issue is particularly critical for aero-engine gas-path fault diagnosis, where different fault modes may produce similar gas-path parameter responses and compound faults are often strongly coupled with single faults [18]. Without structural preservation constraints in the target domain, class confusion and prediction uncertainty may still occur even when the overall source and target distributions are well aligned.

To address the above challenges, this paper proposes a Transferability-Guided Residual Attention Domain Adaptation Network (TG-RADAN) for unsupervised cross-condition fault diagnosis of aero-engines. The proposed method first evaluates the effectiveness of different gas-path features for cross-condition transfer at the input level. A feature Transferability Index is constructed by jointly considering source-domain fault discriminability and cross-domain distribution shift. Based on this index, transferability prior weights are generated to adaptively reweight the input features under transferability guidance, thereby highlighting features that contribute to fault identification while remaining relatively stable across operating conditions. Second, an operating-condition-aware encoder incorporating residual attention and domain-specific batch normalization is developed to enhance the representation of critical fault-related features and mitigate the influence of hidden statistical discrepancies under different operating conditions. Finally, in the deep feature space, conditional adversarial alignment is introduced to reduce the joint distribution discrepancy between the source and target domains, while prototype alignment and entropy minimization are further combined to improve class compactness and prediction confidence in the target-domain feature space.

The main contributions of this paper are summarized as follows:

(1) A Transferability-Guided Residual Attention Domain Adaptation Network (TG-RADAN) is proposed for unsupervised cross-condition gas-path fault diagnosis of aero-engines. The proposed framework integrates input feature reweighting, operating-condition-aware encoding, class-conditional adversarial alignment, and target-domain structure preservation into a unified optimization process, thereby improving diagnostic generalization under complex operating-condition variations.

(2) Unlike conventional global feature alignment strategies that primarily reduce source–target distribution discrepancies in a shared representation space, a Transferability Index (TI) and a TI-guided learnable feature-gating mechanism are developed to explicitly characterize heterogeneous feature transferability before deep domain alignment. The TI jointly considers source-domain fault discriminability and cross-domain distribution

stability, while the learnable gate adaptively regulates the contribution of individual gas-path variables during training, thereby suppressing the adverse influence of operating-condition-sensitive features and reducing the risk of negative transfer.

(3) An operating-condition-aware encoder combining residual attention with domain-specific batch normalization is constructed to enhance the representation of critical fault-related features and alleviate hidden statistical discrepancies across different operating conditions.

(4) A joint constraint incorporating class-conditional adversarial alignment and target-domain structure preservation is introduced to improve the stability of the target-domain class structure and the reliability of diagnostic predictions.

2. Related Work

2.1. Aero-Engine Gas-Path Fault Diagnosis Model

2.1.1. Aero-Engine Gas-Path System and Diagnostic Principles

An aero-engine is a complex propulsion system that integrates aerodynamics, thermodynamic cycles, combustion, and mechanical transmission [19]. The object investigated in this study is a low-bypass-ratio, twin-spool, afterburning turbofan engine, whose cross-sectional view is shown in Figure 1.

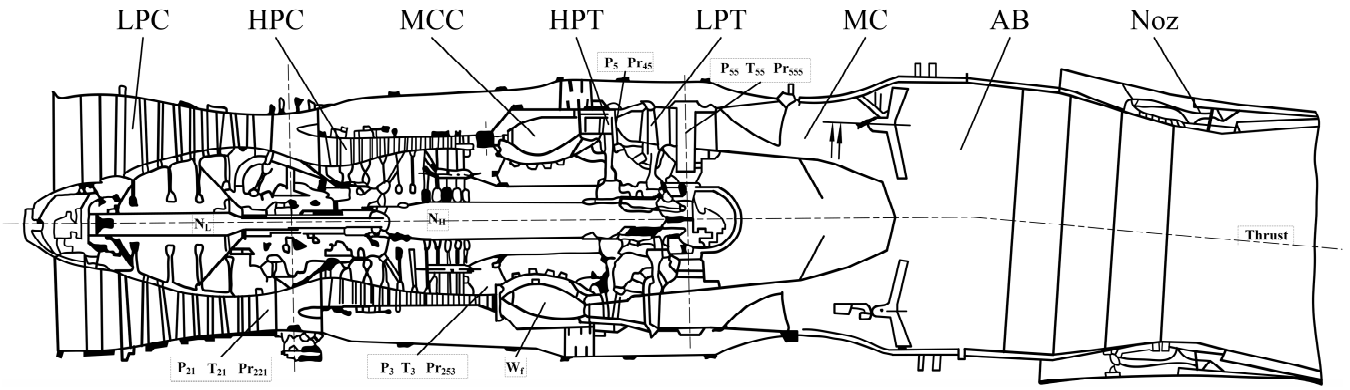


Figure 1. Cross-sectional schematic of the low-bypass-ratio twin-spool afterburning turbofan engine and section-wise parameters considered for gas-path fault diagnosis.

As shown in Figure 1, the main components of the turbofan engine include the low-pressure compressor, high-pressure compressor, main combustor, high-pressure turbine, low-pressure turbine, mixing chamber, afterburner, and exhaust nozzle [20]. These components are tightly coupled through flow continuity, power balance, and thermodynamic matching, and jointly determine the overall operating state of the engine. In addition to illustrating the main gas-path components, Figure 1 also identifies the section-wise parameters considered in the subsequent fault-diagnosis analysis. At the compressor sections, the selected parameters include the total pressure and total temperature at the LPC and HPC outlets, together with the corresponding compressor pressure ratios. At the turbine sections, the total pressure at the HPT outlet, the total pressure and total temperature at the LPT outlet, and the corresponding turbine pressure ratios are considered. The low- and high-pressure spool rotational speeds characterize the operating states of the two mechanically coupled spool systems, while the fuel mass flow rate characterizes the fuel-supply operating condition. Engine thrust is additionally included as an overall performance parameter.

When an aero-engine operates under different altitudes, Mach numbers, and flight attitudes, its working state varies considerably, accompanied by frequent changes in physical characteristics such as rotational speed, pressure, temperature, and load. As a result, gas-path components are more prone to faults than other engine components, posing a

serious threat to flight safety [21]. Meanwhile, during long-term service, faults such as fouling, corrosion, fatigue, and seal damage are often unavoidable. These faults can reduce the thermodynamic performance of gas-path components and further lead to component performance degradation. In the present simulation, these physical damage mechanisms are not modeled as separate fault variables. Instead, their possible effects on gas-path performance are represented at the component-health level through variations in efficiency and flow-capacity parameters. The principle of aero-engine gas-path fault diagnosis is illustrated in Figure 2.

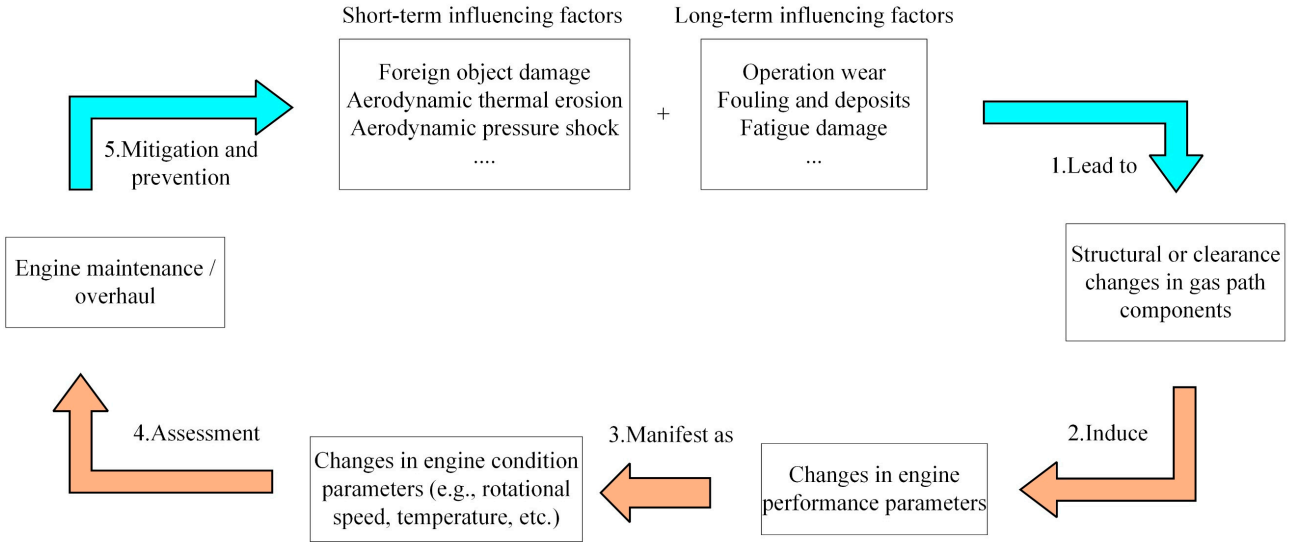


Figure 2. Principle of Aero-Engine Gas-Path Fault Diagnosis.

As shown in Figure 2, aero-engine gas-path faults are mainly caused by various factors, such as foreign object ingestion, aerodynamic and thermal ablation, and service-induced wear, which can be categorized into short-term and long-term influencing factors. These factors may alter the structural characteristics or clearance matching of gas-path components, resulting in component performance degradation, such as reduced compressor efficiency and changes in turbine flow capacity. Such degradation is further reflected in abnormal variations in gas-path performance parameters, including rotational speed and temperature.

Let $\mathcal{H}$ denote the engine health/fault-state space and $\mathcal{Y}$ denote the observation space composed of measurable gas-path performance parameters. The two spaces generally have different dimensions. In the diagnostic task considered in this study, $\mathcal{H}$ contains nine diagnostic states, including the normal state and eight single or compound fault modes, whereas an observation $Y \in \mathcal{Y}$ is composed of the 15 measurable gas-path parameters used as model inputs.

The measurable gas-path response is jointly determined by the component health/fault state and the engine operating condition. Let O denote the operating-condition variable. The forward relationship between the engine state and the measurable gas-path response can therefore be represented as:

$$Y = v(H, O) \tag{1}$$

where $H \in \mathcal{H}$ denotes the engine health/fault state, O represents the operating condition, $Y \in \mathcal{Y}$ denotes the corresponding measurable gas-path observation vector, and $v(\cdot)$ represents the nonlinear forward response of the engine system.

It should be noted that Equation (1) should not be interpreted as a strict one-to-one mapping between a diagnostic fault category and a unique measurement vector. Al-

though a fully specified physical engine state under a fixed operating condition produces a corresponding gas-path response, the same diagnostic fault category may exhibit different measurement vectors under different degradation levels and operating conditions. Therefore, at the fault-category level considered in this study, one health/fault state may correspond to multiple observable gas-path responses.

Conversely, aero-engine gas-path fault diagnosis aims to infer the most likely health/fault state from the measurable gas-path observation. This diagnostic process is represented as:

$$\hat{H} = p(Y) \tag{2}$$

where $\hat{H}$ denotes the predicted engine health/fault state and $p(\cdot)$ denotes the diagnostic mapping learned from data. Unlike the forward engine relationship in Equation (1), $p(\cdot)$ should not be regarded as a strict mathematical inverse of $v(\cdot)$. Instead, it represents a classification or estimation process that maps the measurable gas-path parameters to the most probable health/fault category.

2.1.2. Gas-Path Fault Diagnosis Model for Aero-Engines

Existing techniques for aero-engine gas-path fault diagnosis can generally be classified into two categories: model-based and data-driven approaches [22]. This study adopts a data-driven fault diagnosis model, which avoids the need for complex mathematical modeling and instead builds an efficient and accurate diagnostic model by exploiting historical data. The data-driven fault diagnosis model for the aero-engine gas-path system can be formulated as

$$Z = F(X), \tag{3}$$

where $Z = [z_1, z_2, \cdots, z_n]$ denotes the output of the fault diagnosis model, where $z_i (i = 1, 2, \cdots n)$ represents the fault modes of the gas-path system. $X = [x_1, x_2, \cdots, x_j]$ denotes the input of the fault diagnosis model, where $x_j (j = 1, 2, \cdots n)$ represents the measured sensor parameters of the aero-engine. $F(\cdot)$ represents the nonlinear mapping relationship between X and Z.

Most existing data-driven diagnostic models are still built on the assumption that the training and testing data are independent and identically distributed. However, this assumption is often violated in practical aero-engine operation. Since variations in altitude and Mach number across operating conditions can substantially change the distribution of gas-path data, a diagnostic model trained under one operating condition is difficult to transfer directly to another. Although data-driven methods have improved fault recognition capability, their cross-condition generalization ability remains limited, which has motivated increasing research on transfer learning and unsupervised domain adaptation in this field.

2.2. Transfer Learning and Unsupervised Domain Adaptation

Transfer learning improves model generalization and adaptability by transferring knowledge learned from a source domain to a target domain, thereby reducing the reliance on large-scale labeled data [23]. In aero-engine gas-path fault diagnosis, fault samples are difficult and costly to annotate, making transfer learning a promising technical pathway for cross-condition fault diagnosis. In particular, unsupervised domain adaptation requires only labeled source-domain data and unlabeled target-domain data, which better matches the practical requirements of aero-engine cross-condition diagnosis [24].

As a representative cross-domain transfer paradigm, unsupervised domain adaptation (UDA) aims to address distribution discrepancies between the labeled source domain and the unlabeled target domain [25]. Existing UDA methods can generally be grouped into three categories: distribution-metric-based approaches, adversarial domain adapta-

tion, and class-conditional structural constraints. Distribution-metric-based approaches reduce statistical discrepancies between domains using measures such as maximum mean discrepancy (MMD), correlation alignment (CORAL), Wasserstein distance, and joint distribution discrepancy. Adversarial domain adaptation introduces a domain discriminator to encourage the feature extractor to learn domain-invariant representations, with typical domain-adversarial methods achieving domain confusion through a gradient reversal mechanism and showing strong adaptability to nonlinear cross-domain tasks. Class-conditional structural constraint methods further promote joint-distribution-level alignment by incorporating classification predictions, pseudo-labels, and consistency regularization.

Despite their effectiveness, conventional global feature alignment strategies generally impose distribution-matching constraints on the overall feature representation without explicitly evaluating the heterogeneous transferability of individual input variables before alignment. This limitation is particularly relevant to aero-engine gas-path diagnosis because different gas-path parameters exhibit markedly different sensitivities to fault degradation and operating-condition variations. Consequently, directly aligning representations constructed from all input variables may allow strongly condition-sensitive features to participate in the transfer process together with relatively stable and fault-discriminative features, thereby increasing the risk of negative transfer. In contrast, the proposed TI introduces an explicit feature-wise transferability assessment prior to deep domain alignment by jointly considering source-domain fault discriminability and cross-domain distribution stability. Features that are both more discriminative for fault identification and relatively stable across operating conditions are assigned higher transferability priors. Furthermore, rather than using these priors as fixed weights, TG-RADAN incorporates them into a learnable gating mechanism so that the contribution of each gas-path variable can be adaptively refined during end-to-end optimization. Therefore, the TI-guided mechanism does not replace conventional representation-level domain alignment; instead, it complements subsequent class-conditional alignment by regulating heterogeneous feature transferability at the input level, resulting in a hierarchical adaptation strategy from feature-level reweighting to latent-space distribution alignment.

3. Proposed Method

3.1. Overview

Aero-engine gas-path feature parameters often exhibit substantial distribution discrepancies across operating conditions, and different features show unequal degrees of shift during cross-condition transfer. Most existing domain adaptation methods implicitly assume comparable domain-shift characteristics among all features and thus perform unified modeling and global alignment over the entire feature space. This assumption makes it difficult to characterize the heterogeneous transferability of gas-path features under operating-condition variations. Consequently, operating-condition-sensitive features may be mistakenly involved in cross-domain alignment, causing negative transfer and degrading diagnostic performance.

To overcome these limitations, a Transferability-Guided Residual Attention Domain Adaptation Network (TG-RADAN) is proposed for unsupervised cross-condition gas-path fault diagnosis of aero-engines. TG-RADAN is designed to improve cross-condition transfer diagnosis through four coordinated modules: input reweighting, operating-condition-aware encoding, class-conditional alignment, and target-domain structure preservation. The overall architecture of the proposed model is illustrated in Figure 3.

As shown in Figure 3, TG-RADAN mainly consists of the following four core modules.

(1) **Transferability-guided feature reweighting module.** To address the heterogeneous domain-shift characteristics of different gas-path features under cross-condition scenarios,

a feature Transferability Index (TI) is first constructed to comprehensively measure the fault discriminability of each input feature in the source domain and its distribution stability across operating conditions. Based on the TI, a TI-guided learnable feature-gating mechanism is introduced to adaptively reweight each input feature. In this way, stable and discriminative transfer-critical features are highlighted at the input level, while high-risk operating-condition-sensitive features are suppressed to reduce their interference with subsequent training and alleviate negative transfer.

(2) **Residual-attention operating-condition-aware encoding module.** For the gated input features, a residual-attention feature encoder is further constructed to enhance the nonlinear representation capability of gas-path features while maintaining a lightweight network structure. The encoder consists of an input mapping layer, residual fully connected transformations, feature attention units, and domain-specific batch normalization. Specifically, residual connections are used to alleviate representation degradation during deep feature mapping; feature attention adaptively enhances key hidden features related to fault diagnosis and cross-domain transfer; and DSBN separately models the statistical characteristics of the source and target domains, thereby improving the stability and consistency of representation learning under operating-condition variations.

(3) **Class-conditional adversarial domain alignment module.** After operating-condition-aware deep features are obtained, the classification branch preserves the discriminative structure of source-domain fault classes, while the conditional domain alignment module aligns the feature distributions of the source and target domains under class-conditional constraints. Unlike methods that only align marginal distributions, this study incorporates class prediction information into the domain discrimination process, making cross-domain alignment closer to joint distribution matching and effectively reducing the risk of class confusion in cross-condition scenarios.

(4) **Target-domain structure preservation module.** Relying solely on adversarial distribution alignment may still cause target-domain samples to lie close to decision boundaries, resulting in class overlap and prediction uncertainty. To further stabilize the transfer process, structural regularization constraints are introduced. Prototype alignment uses source-domain class prototypes to guide high-confidence target samples toward their corresponding class clusters, thereby maintaining the consistency of class geometry in the cross-domain feature space. Entropy minimization increases the prediction confidence of target-domain samples and pushes decision boundaries away from high-density regions of the target domain, thus enhancing the certainty and robustness of target-domain predictions.

Rather than operating as a simple combination of independent modules, TG-RADAN follows a hierarchical adaptation strategy in which different components address cross-condition domain shift at complementary levels. At the input-feature level, TI-guided learnable gating first regulates heterogeneous gas-path variables according to their fault discriminability and cross-domain stability, thereby providing more transferable inputs for subsequent representation learning. At the representation and statistical level, the residual-attention encoder captures nonlinear coupling relationships among gas-path variables, while DSBN separately models source- and target-domain activation statistics to reduce hidden statistical discrepancies. Based on these more stable representations, conditional adversarial alignment further reduces class-conditional distribution discrepancies between the two domains at the latent-feature level. Finally, prototype alignment and entropy minimization operate at the target-structure level to preserve class-wise geometric consistency and improve prediction confidence, compensating for the inability of adversarial alignment alone to guarantee a well-structured target distribution. These modules are jointly optimized in an end-to-end manner, so that downstream classification, domain-alignment, and structural-regularization objectives can also adaptively influence the TI-guided feature-

gating process. Consequently, TG-RADAN establishes a progressive adaptation pathway from input-level transferability regulation, through representation-level statistical adaptation and class-conditional distribution alignment, to target-domain structural preservation, rather than simply stacking multiple domain adaptation components.

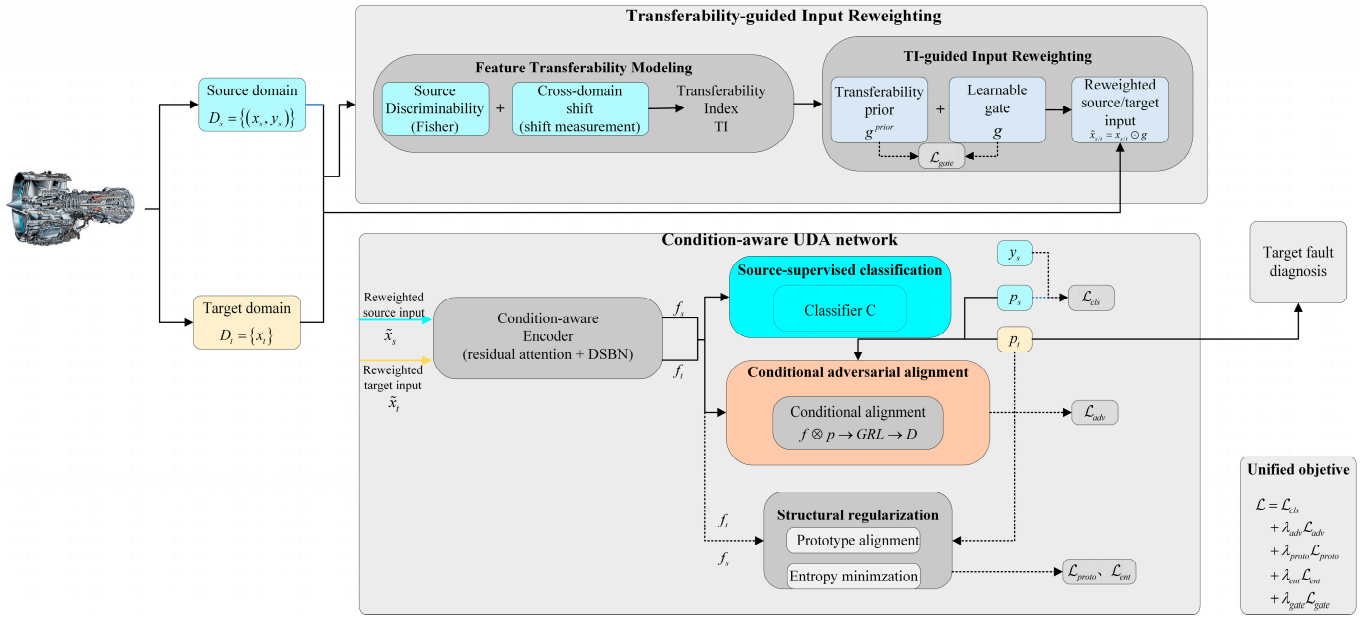


Figure 3. Overall Framework of TG-RADAN for Unsupervised Cross-Condition Fault Diagnosis.

3.2. Transferability-Guided Input Reweighting for TG-RADAN

In cross-condition aero-engine gas-path fault diagnosis, domain shift does not affect all features uniformly. Owing to the characteristics of thermodynamic cycles, aerothermodynamic mechanisms, and the coupling of operating states, different gas-path feature parameters exhibit heterogeneous domain-shift behaviors under operating-condition variations. Some features can maintain relatively high stability and fault discriminability across different operating conditions, whereas others exhibit relatively larger distribution shifts between operating conditions and may therefore introduce stronger condition-specific discrepancies during cross-condition transfer.

In the TG-RADAN model, transferability modeling is first performed at the input level. Considering the heterogeneous cross-condition shifts of aero-engine gas-path features, treating all standardized input features uniformly may cause operating-condition-sensitive features to receive disproportionate emphasis during representation learning, thereby introducing excessive condition-specific information and increasing the risk of negative transfer. It should be noted that input standardization only reduces numerical scale differences among heterogeneous gas-path parameters and does not eliminate the source–target distribution shift associated with operating-condition variations. Therefore, the proposed reweighting mechanism operates on the relative transferability of standardized features rather than compensating for their original physical magnitudes. Based on this consideration, a transferability-guided input reweighting mechanism is incorporated at the input end of TG-RADAN. By constructing a feature Transferability Index (TI), the transfer potential of each gas-path feature is evaluated. Furthermore, using the TI as a prior, a learnable gating mechanism is designed to adaptively regulate each input feature, providing more stable and transferable input representations for subsequent residual-attention encoding and class-conditional adversarial alignment.

3.2.1. Transferability Index

To quantify the fault-discriminative capability of each gas-path feature, the Fisher score is employed as an evaluation criterion [26]. The Fisher score evaluates the separability of a feature by comparing its between-class dispersion with its within-class dispersion in the labeled source domain. For the d-th gas-path feature, it is defined as follows:

$$F_d = \frac{\sum_{c=1}^{C} \pi_c \left(\mu_{d,c}^s - \mu_d^s\right)^2}{\sum_{c=1}^{C} \pi_c \left(\sigma_{c,d}^2\right)^2 + \varepsilon}, \tag{4}$$

where C denotes the number of fault categories and d denotes the feature index. Let n_s denote the total number of source-domain training samples and n_c^s denote the number of source-domain samples belonging to class c. The empirical class prior is calculated as: $\pi_c = \frac{n_c^s}{n_s}$. $\mu_{d,c}^s$ and $\left(\sigma_{d,c}^s\right)^2$ denote the mean and variance of the d-th feature for class c in the source domain. μ_d^s denotes the overall mean of the d-th feature in the source domain, and ε is a numerical stability term. A larger F_d indicates stronger discriminative capability of the feature in distinguishing different fault categories in the source domain.

Different from the discriminative capability measured by the Fisher score, highly transferable gas-path features are expected to remain insensitive to operating-condition variations. To quantify the transferability of different gas-path features, this study proposes a cross-domain shift metric, defined as follows:

$$\Delta_d^{s \to t} = \frac{\left|\mu_d^s - \mu_d^t\right|}{\sigma_d^s + \sigma_d^t + \varepsilon}, \tag{5}$$

where μ_d^s, μ_d^t denote the mean values of the d-th feature in the source and target domains, and σ_d^s, σ_d^s denote the corresponding standard deviations. This metric reflects the normalized mean shift of features under different operating conditions. A larger Δ_d indicates higher sensitivity of the feature to operating-condition variations.

For each cross-condition transfer task, this metric is calculated independently for all gas-path features using the source-domain and unlabeled target-domain training data. The operating-condition sensitivity is evaluated comparatively: features with larger cross-domain shift values are regarded as relatively more sensitive to the operating-condition variation between the corresponding source and target domains. No fixed threshold is introduced to divide the features into sensitive and insensitive groups because the degree of distribution shift is continuous and may vary among different transfer tasks. Instead, this metric is subsequently incorporated into the TI as a continuous shift penalty. Accordingly, features with relatively larger values of this metric are interpreted as exhibiting stronger feature-wise contributions to the observed cross-condition discrepancy; this interpretation is comparative and does not represent an additive decomposition of the overall domain discrepancy.

Based on Equations (4) and (5), the Transferability Index (TI) is defined as follows:

$$\mathrm{TI}_d = \mathcal{N}(\alpha F_d - \beta \Delta_d), \mathcal{N}(x) = \frac{x - x_{\min}}{x_{\max} - x_{\min}}, \tag{6}$$

where α and β are the discriminative reward coefficient and shift penalty coefficient, and $\mathcal{N}(\cdot)$ denotes a normalization function.

The overall construction process of the Transferability Index is illustrated in Figure 4.

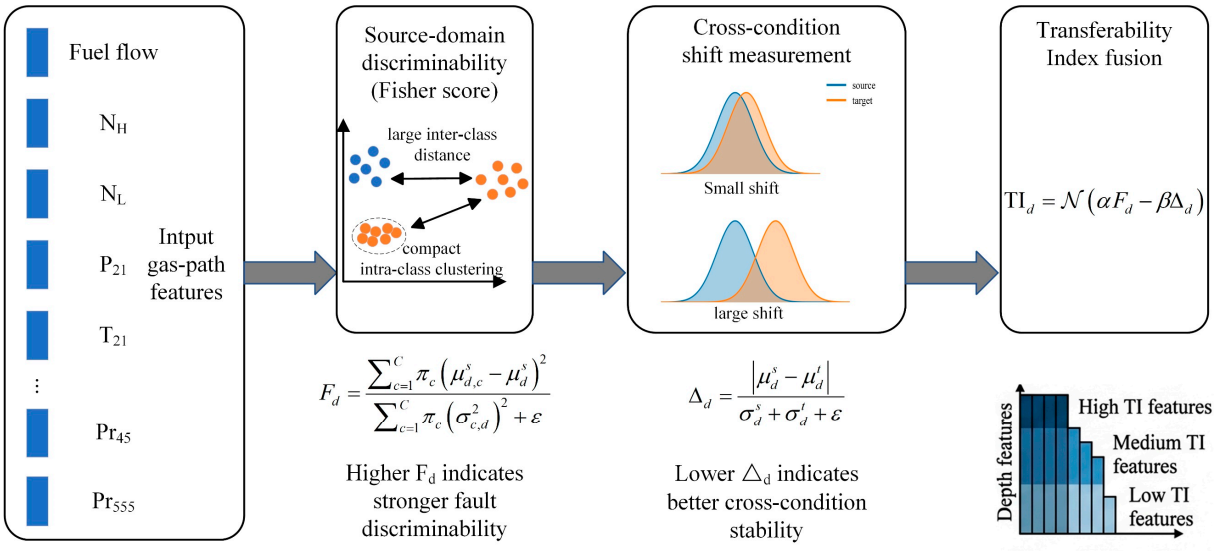


Figure 4. Construction process of the Transferability Index.

3.2.2. TI-Guided Learnable Gating

The Transferability Index (TI) provides a principled prior for feature transferability. Nevertheless, static feature reweighting may restrict the model's adaptability during training. As the feature extractor and classifier are iteratively updated, the relative importance of different gas-path features for fault discrimination and domain alignment may vary accordingly. Moreover, optimization objectives such as domain-adversarial alignment introduce reverse-gradient signals, which require the model to dynamically adjust the contribution of each feature.

To this end, this study develops a TI-guided learnable feature-gating mechanism that enables adaptive regulation of individual input features according to the training objectives. The schematic of the TI-guided learnable gating mechanism is shown in Figure 5.

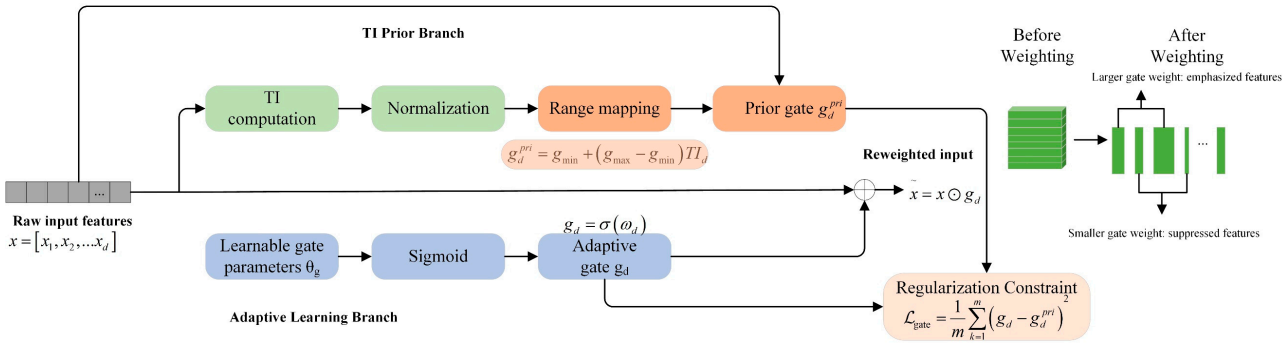


Figure 5. Schematic Diagram of the TI-Guided Learnable Gating Mechanism.

Let the original input feature be $x \in \mathbb{R}^m$, and the gated input be denoted as $\tilde{x} \in \mathbb{R}^m$, then:

$$\tilde{x} = x \odot g, \tag{7}$$

where $g \in \mathbb{R}^m$ denotes the feature gating vector, defined as $g = [g_1, g_2, \cdots g_m]$. $\odot$ represents the Hadamard product, i.e., $(x \odot g)_1 = x_1 g_1$, and $\mathbb{R}^m$ denotes an m-dimensional real-valued vector space.

Based on the Transferability Index (TI), the prior gating weights are formulated as:

$$g_d^{pri} = g_{\min} + (g_{\max} - g_{\min}) TI_d, \tag{8}$$

where $g_{\min}$ and $g_{\max}$ denote the lower and upper bounds of gating weights, which are used to constrain the weighting range and prevent excessive amplification or complete suppression of features.

It should be noted that the proposed gating operation performs feature-wise rescaling rather than feature decorrelation. For a given transfer task, the same learnable gating vector is shared by all samples from both the source and target domains, and its elements are constrained to positive values. Therefore, the gating mechanism adjusts the relative contribution of individual gas-path variables without explicitly removing the statistical dependencies among them.

On this basis, the final learnable gating weights are obtained by mapping the parameter ω_d through a Sigmoid function:

$$g_d = g_{\min} + (g_{\max} - g_{\min})\sigma(\omega_d), \tag{9}$$

where $\sigma(\cdot)$ denotes the Sigmoid activation function.

To prevent the learnable gating mechanism from deviating excessively from the TI-induced transferability prior during optimization, a regularization term is introduced:

$$\mathcal{L}_{\text{gate}} = \frac{1}{m}\sum_{k=1}^{m}\left(g_d - g_d^{pri}\right)^2, \tag{10}$$

This constraint does not enforce strict equality between the learnable weights and the prior, but instead penalizes excessive deviation, thereby preserving adaptive flexibility while improving interpretability and stability of the feature reweighting process.

3.3. Condition-Aware Representation and Conditional Alignment

This section details the operating-condition-aware representation learning and conditional alignment mechanisms of TG-RADAN. For the features reweighted by TI-guided gating, the model aims to learn deep representations that are transferable, robust, and fault-discriminative across operating conditions, while achieving class-conditional distribution alignment and structural preservation between the source and target domains. To this end, TG-RADAN collaboratively employs five core modules in the feature encoding and domain adaptation stages: residual-attention-based operating-condition-aware encoding, domain-specific batch normalization, source-domain supervised classification, conditional adversarial alignment, and structural regularization constraints.

3.3.1. Residual Attention-Based Condition-Aware Encoder

Aero-engine gas-path feature parameters are not independent of each other but are jointly influenced by component mass flow variations, efficiency degradation, and the overall aero-thermodynamic relationships, exhibiting strong coupling characteristics [27]. Therefore, relying solely on conventional fully connected mappings for feature extraction is insufficient to fully capture the nonlinear interactions among features. To enhance the feature representation capability, a residual attention-based condition-aware encoder is constructed on top of the TI-guided reweighted inputs, which is designed to extract more stable and highly discriminative deep representations. The schematic diagram of the proposed architecture is shown in Figure 6.

In this study, the operating condition is characterized by flight altitude and Mach number. Four representative operating conditions, denoted as A–D, are considered, as described below. For each cross-condition transfer task, data under one operating condition are treated as the source domain, whereas data under another operating condition are treated as the target domain. It should be noted that altitude and Mach number are

used to define the operating-condition domains rather than being directly concatenated with the 15-dimensional gas-path measurement vector as additional encoder inputs. The operating-condition-aware capability of the encoder is mainly realized through adaptive feature recalibration and domain-specific statistical modeling. Specifically, the attention mechanism adaptively adjusts hidden feature responses, while DSBN separately models the normalization statistics of the source and target operating-condition domains.

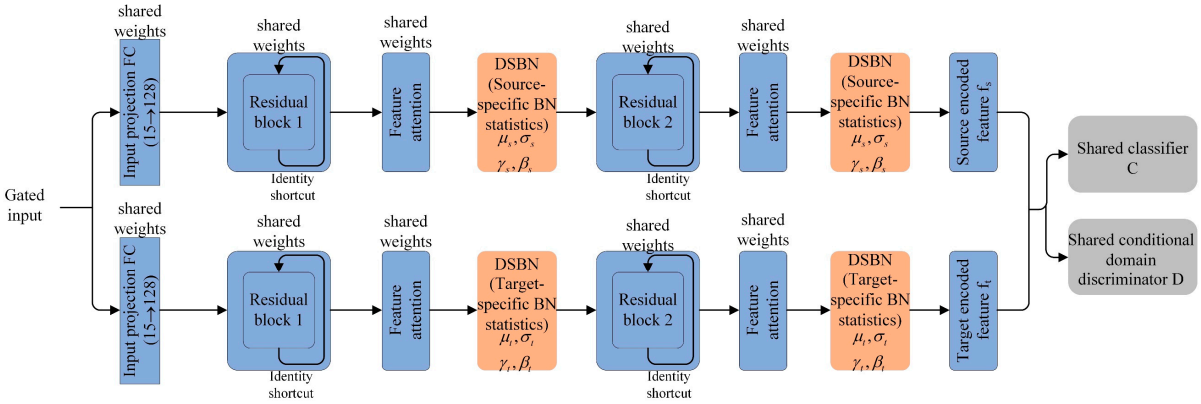


Figure 6. Residual Attention Encoder with DSBN.

This gated input feature is denoted as source-domain samples $\widetilde{x}_s$ and target-domain samples $\widetilde{x}_t$, and the feature encoder is defined as $G_f(\cdot)$. Unlike conventional shallow fully connected networks, the proposed encoder adopts a residual attention-based architecture composed of an input projection layer, multi-stage residual fully connected transformations, and feature-level attention units. This design aims to model the inherent nonlinear coupling relationships among aero-engine gas-path variables while mitigating representation degradation through residual learning.

In cross-condition aero-engine fault diagnosis, different hidden-layer representations exhibit inconsistent sensitivities to fault-related variations and operating-condition disturbances, which limits the robustness of deep feature learning under domain shift.

To address this issue, a residual attention-based condition-aware encoding strategy is introduced. Specifically, at each transformation stage, an attention mechanism is applied to adaptively recalibrate feature responses across different dimensions, enabling the network to emphasize informative fault-related components while suppressing condition-sensitive variations.

Formally, the encoder begins with an input projection mapping:

$$h^{(0)} = \phi(W_0\widetilde{x} + b_0), \tag{11}$$

where W_0 and b_0 denote the projection weight matrix and bias vector, $\phi(\cdot)$ represents the nonlinear activation function, and $h^{(0)}$ is the initial hidden representation.

For the l-th residual transformation stage, the output $h^{(l-1)}$ of the previous stage is directly taken as the input of the current stage and is first processed through the following nonlinear mapping:

$$z^{(l)} = \phi\left(W_l h^{(l-1)} + b_l\right), \tag{12}$$

where W_l and b_l are the parameters of the l-th layer, and $h^{(l-1)}$ denotes the output of the previous stage.

A residual connection is then introduced to preserve low-level information and stabilize deep feature propagation:

$$r^{(l)} = h^{(l-1)} + z^{(l)} \tag{13}$$

Here, $h^{(l-1)}$ is transmitted through the identity shortcut, while its nonlinear transformation $z^{(l)}$ forms the residual branch; the two branches are combined by element-wise addition to obtain $r^{(l)}$. In cross-condition aero-engine gas-path fault diagnosis, the sensitivities of different hidden-layer responses to fault representation and operating-condition variations are not consistent. To enhance the encoder's adaptability to such discrepancies, a feature attention mechanism is introduced at each residual transformation stage to adaptively reweight the hidden-layer dimensions [28]. The attention weight vector is defined as follows:

$$a^{(l)} = \sigma\left(W_a^{(l)} r^{(l)} + b_a^{(l)}\right), \tag{14}$$

where $W_a^{(l)}$ and $b_a^{(l)}$ are attention unit parameters, and $a^{(l)}$ denotes the element-wise attention weight vector.

The recalibrated representation is obtained via:

$$h^{(l)} = a^{(l)} \odot r^{(l)}, \tag{15}$$

The recalibrated representation $h^{(l)}$ constitutes the output of the l-th residual-attention stage and is directly propagated as the input to the next stage. Specifically, for the $(l+1)$-th stage, $h^{(l)}$ replaces $h^{(l-1)}$ in Equation (12), after which the nonlinear transformation, residual addition, and attention recalibration described by Equations (12)–(15) are repeated. Therefore, the layer-to-layer propagation of the encoder follows the recursive sequence $h^{(l-1)} \to z^{(l)} \to r^{(l)} \to a^{(l)} \to h^{(l)}$, with $h^{(l)}$ serving as the input of the subsequent stage.

After L residual attention stages, the final deep feature representation is formulated as:

$$f = h^{(L)}, \tag{16}$$

where L denotes the number of residual attention stages, set to $L = 2$ in this study.

Overall, the proposed residual attention encoder enhances feature discrimination by explicitly modeling nonlinear feature coupling, while adaptively suppressing condition-sensitive disturbances through attention-based recalibration. This results in more stable and transferable representations for subsequent domain alignment and fault classification tasks.

3.3.2. Domain-Specific Batch Normalization for Condition-Aware Representation

In cross-condition aero-engine gas-path fault diagnosis, significant statistical discrepancies exist between source and target domains due to variations in operating conditions such as altitude and Mach number. Directly sharing batch normalization statistics across domains may introduce distribution bias and degrade representation stability.

To address this issue, domain-specific batch normalization (DSBN) is embedded into each layer of the encoder. DSBN maintains separate normalization statistics and affine transformation parameters for the source and target domains while sharing the remaining network parameters. This design enables the model to explicitly capture domain-specific statistical properties while preserving a unified feature extraction backbone. Therefore, in each cross-condition transfer task, the source and target DSBN branches respectively characterize the hidden activation statistics associated with the two different operating conditions.

Specifically, the source- and target-domain samples follow the same feature-transformation process in the shared encoder $G(\cdot)$, but their intermediate activations are passed through different DSBN branches according to the domain index d. The source-domain activations are normalized by $DSBN_s$, whereas the target-domain activations are normalized by $DSBN_t$. Therefore, the two domains share the encoder parameters θ but maintain independent

BN statistics and affine parameters. Formally, for an intermediate activation u, the DSBN transformation under domain $d \in \{s, t\}$ is defined as:

$$DSBN_d(u) = \gamma_d \odot \frac{u - \mu_d}{\sqrt{\sigma_d^2 + \varepsilon}} + \beta_d, \tag{17}$$

where μ_d and σ_d^2 denote the mean and variance of domain d, γ_d and β_d are domain-specific learnable scaling and shifting parameters, and ε is a numerical stability term. More specifically, let B_d denote the number of samples from domain d in the current mini-batch, and let $u_{d,i}$ denote the intermediate activation of the i-th sample from domain d. The domain-specific batch statistics in Equation (17) are calculated as $\mu_d = \frac{1}{B_d}\sum_{i=1}^{B_d} u_{d,i}$, $\sigma_s^2 = \frac{1}{B_d}\sum_{i=1}^{B_d}(u_{d,i} - \mu_d)^2$.

Accordingly, the shared encoder produces domain-specific feature representations:

$$f_s = G(\widetilde{x_s}; \theta, DSBN_s),\ f_t = G(\widetilde{x_t}; \theta, DSBN_t), \tag{18}$$

where $G(\cdot)$ denotes the shared feature encoder and θ represents shared parameter.

By embedding DSBN at each stage of the encoder, TG-RADAN separately captures the statistical characteristics of the source and target domains under different operating conditions, thereby reducing the interference of cross-domain statistical entanglement in feature extraction. This provides a more stable representation foundation for subsequent class-conditional adversarial alignment and structure preservation.

3.3.3. Supervised Classification and Conditional Adversarial Alignment

To ensure that the learned fault representations possess strong discriminative capability, a supervised classification branch is introduced on the source-domain features. Let the classifier be $C(\cdot)$, and the predicted probability vector of a sample is given by:

$$p_s = C(f_s),\ p_t = C(f_t), \tag{19}$$

where $p_s,\ p_t \in \mathbb{R}^C$ denotes the predicted probability distribution over C fault categories for source- and target-domain samples, respectively. The source prediction p_s is used for supervised classification with the available source labels, whereas both p_s and p_t are subsequently used in conditional adversarial alignment.

With source-domain label supervision, the classification loss is defined as:

$$\mathcal{L}_{cls} = -\frac{1}{N_s}\sum_{i}^{N_s}\sum_{c=1}^{C} y_{i,c}^s \log p_{i,c}^s, \tag{20}$$

where $y_{i,c}^s$ is the indicator variable for source sample i belonging to class c, and $p_{i,c}^s$ is the corresponding predicted probability.

With source-domain label supervision, the classifier is optimized using the cross-entropy loss, which encourages samples from different fault classes to form well-separated discriminative structures in the feature space. This classification loss not only enhances source-domain fault recognition, but also provides reliable supervision for subsequent conditional adversarial alignment and structural regularization.

Although adversarial domain adaptation can mitigate the distribution discrepancy between the source and target domains, marginal distribution alignment alone is prone to class confusion under severe cross-condition shifts. In gas-path fault diagnosis, the same fault may present substantially different representations across operating conditions,

while different faults may produce similar response patterns under certain conditions. Consequently, marginal alignment may incorrectly reduce the distance between samples from different classes in the feature space, leading to degraded diagnostic performance.

To address this issue, this study adopts conditional adversarial domain adaptation (CDAN), which performs domain alignment under class-conditional constraints to better approximate joint distribution matching and preserve class structures [29]. The conditional representation is constructed as follows:

$$g = T(f, p) = f \otimes p, \tag{21}$$

where $\otimes$ denotes the outer product between the feature representation and the class-probability vector. $T(\cdot)$ denotes the conditional mapping function, which is used to fuse deep feature representations with class prediction information.

A learnable binary domain discriminator $D(\cdot)$ is then introduced to identify the domain origin of each conditional representation. Specifically, D maps the condition feature g_i to a scalar domain logit. The adversarial loss is defined as:

$$\mathcal{L}_{adv} = -\frac{1}{N_s + N_t} \sum_{i=1}^{N_s+N_t} [d_i \log D(g_i) + (1 - d_i) \log(1 - D(g_i))], \tag{22}$$

where $d_i \in \{0, 1\}$ denotes the domain label, with 1 indicating the source domain and 0 indicating the target domain.

To achieve adversarial optimization, a gradient reversal layer (GRL) is introduced between the conditional feature representation and the domain discriminator. Specifically, the domain discriminator is trained to minimize $\mathcal{L}_{adv}$, while the feature encoder receives reversed gradients through the GRL to learn domain-invariant representations with stronger condition generalization capability. This adversarial learning strategy effectively reduces the distribution discrepancy under different operating conditions and mitigates the risk of confusion between different fault categories during alignment.

3.3.4. Structural Regularization for Target-Domain Stability

Although conditional adversarial alignment effectively mitigates the distribution discrepancy between the source and target domains, it does not explicitly ensure the stability of the target-domain class structure. Under large operating-condition discrepancies, adversarial training alone may still result in class overlap and prediction uncertainty. To alleviate these issues, TG-RADAN incorporates a structural regularization strategy that imposes auxiliary loss constraints on feature representations and prediction outputs without altering the network's forward propagation structure [30]. Two complementary regularization terms are employed: prototype alignment to preserve the consistency of class-wise geometric structures, and entropy minimization to enhance the certainty of target-domain predictions.

(1) Prototype Alignment

In fault diagnosis tasks, samples from the same fault category are expected to form compact clusters in the feature space. However, alignment methods that primarily enforce domain consistency may, to some extent, distort the intrinsic geometric structure of class distributions. To preserve intra-class compactness and inter-class separability in the feature space, a prototype alignment strategy is introduced, where class prototypes from the source domain are used as stable class anchors to guide the distribution of target-domain features.

For the c-th, the source-domain class prototype is defined as the mean feature representation of all source samples belonging to that class:

$$\mu_c = \frac{1}{|S_c|} \sum_{x_i^s \in S_c} f_i^s, \tag{23}$$

where S_c denotes the set of source samples in class c, $|S_c|$ is the number of samples in this set, and f_i^s represents the feature embedding of the i-th source sample.

Since the target domain is unlabeled in unsupervised fault diagnosis, pseudo-labels are generated using classifier predictions. To reduce label noise, only target samples with high prediction confidence are selected for prototype alignment.

For a target sample x_j^t, its pseudo-label is defined as:

$$\hat{y}_j^t = \underset{c}{\text{argmax}}\ p_{j,c}^t \ , \max_c p_{j,c}^t > \tau, \tag{24}$$

where τ is confidence threshold.

Accordingly, the prototype alignment loss is formulated as:

$$\mathcal{L}_{proto} = \frac{1}{|\tau_h|} \sum_{x_j^t \in \tau_h} \left\| f_j^t - \mu_{\hat{y}_j^t} \right\|_2^2, \tag{25}$$

where $|\tau_h|$ denotes the set of high-confidence target samples.

(2) Entropy Minimization

Despite the incorporation of adversarial alignment and prototype constraints, uncertainty may still exist in target-domain predictions, particularly for samples near decision boundaries. To further encourage confident predictions, an entropy minimization strategy is introduced. The prediction entropy for a target sample is defined as:

$$H\left(p_j^t\right) = -\sum_{c=1}^{C} p_{j,c}^t \log p_{j,c}^t \tag{26}$$

The corresponding entropy minimization loss is formulated as:

$$\mathcal{L}_{ent} = \frac{1}{N_t} \sum_{j=1}^{N_t} H\left(p_j^t\right) \tag{27}$$

The prototype alignment strategy preserves class-level geometric consistency in the feature space by enforcing intra-class compactness guided by source-domain class prototypes. Meanwhile, entropy minimization encourages the model to produce more confident and discriminative predictions in the target domain. The combination of these two strategies improves the reliability and stability of unsupervised cross-condition aero-engine fault diagnosis.

3.3.5. Overall Objective

Combining all the aforementioned loss terms, the overall optimization objective of this study is defined as:

$$\mathcal{L} = \mathcal{L}_{cls} + \lambda_{adv}\mathcal{L}_{adv} + \lambda_{proto}\mathcal{L}_{proto} + \lambda_{ent}\mathcal{L}_{ent} + \lambda_{gate}\mathcal{L}_{gate}, \tag{28}$$

where λ_{adv}, λ_{ptoto}, λ_{ent} and λ_{gate} denote the weighting coefficients for the adversarial loss, prototype alignment loss, entropy minimization loss, and gating regularization term, respectively.

Under this unified optimization framework, $\mathcal{L}_{cls}$ is used to preserve the discriminative structure of fault categories, $\mathcal{L}_{adv}$ reduces conditional distribution discrepancies across operating conditions, $\mathcal{L}_{proto}$ and $\mathcal{L}_{ent}$ jointly enhance target-domain structural compactness and prediction confidence, while $\mathcal{L}_{gate}$ regulates the feature reweighting behavior at the input level. Through this multi-objective collaborative optimization, the proposed model achieves effective cross-condition aero-engine gas-path fault diagnosis under unsupervised settings. Accordingly, the overall objective couples feature-level transferability regulation with representation learning, domain alignment, and target-structure preservation, enabling the different components of TG-RADAN to be optimized cooperatively rather than as independent processing stages.

4. Experimental Analysis

4.1. Experimental Configuration

4.1.1. Gas-Path Data Preparation for Aero-Engine

This study focuses on the application of transfer learning to unsupervised aero-engine gas-path fault diagnosis; therefore, gas-path faults are the primary research object. Changes in the flow capacity and efficiency of gas-path components are direct manifestations of aero-engine gas-path faults. However, in practical operation, the efficiency and flow capacity of individual components are difficult to measure directly. Such changes are reflected in measurable engine parameters, including rotational speed, temperature, and pressure, which characterize the operating state and performance behavior of the engine. Accordingly, by analyzing the variation trends and abnormal patterns of these measurable parameters, potential fault types in gas-path components can be indirectly inferred [31].

Considering the relevance of health parameters to gas-path components and their diagnostic importance, 15 parameters are selected in this study, as listed in Table 1. The component fault-severity settings adopted in this study are specified in terms of relative variations in component efficiency and flow-capacity health parameters. The variation magnitudes listed in Table 2 are referenced to the C-MAPSS study reported by DeCastro et al. [32] and are used as reference perturbation levels for constructing the fault conditions in the present component-level aerothermodynamic model.

During aero-engine service, engine performance gradually degrades as operating time increases. When the degradation reaches a certain level, the normal operation of the engine may be affected, indicating that the engine has reached the end of its service life [33]. During the degradation process, engines with different degradation levels exhibit different performance characteristics; therefore, the operating data collected from engines at different degradation levels follow different distributions. In this study, operating data are generated for both the nominal engine and mildly degraded but non-fault engine conditions. For each gas-path component k, the degradation is introduced relative to its nominal efficiency coefficient η_k^0, and the degraded efficiency coefficient is expressed as $\eta_k = \eta_k^0(1 - \delta_k)$, where δ_k denotes the relative efficiency degradation. For the LPC, HPC, HPT, and LPT, multiple mild degradation levels within the range of 0.1–0.5% are considered to introduce realistic performance dispersion while maintaining normal engine operation. These mild efficiency perturbations are distinguished from the fault-level health-parameter variations listed in Table 2, which are used to construct the corresponding component fault modes.

It should be emphasized that the degradation introduced in this study is prescribed at the component-health-parameter level rather than by independently perturbing the measurable gas-path variables. The component efficiency parameters are used to characterize slight background performance degradation of the LPC, HPC, HPT, and LPT. Once a degradation level is specified, the corresponding gas-path responses are obtained from the nonlinear component-level aero-thermodynamic engine model. Therefore, rotational

speeds, pressures, temperatures, fuel flow, pressure ratios, and thrust are treated as coupled responses of the engine operating state rather than independently modified variables.

Table 1. Input Feature Parameters for Aero-Engine Gas-Path Fault Diagnosis.

Symbol	Parameter	Unit
W_f	Fuel mass flow rate	kg/s
N_H	High-pressure spool rotational speed	RPM
N_L	Low-pressure spool rotational speed	RPM
P_{21}	Total pressure at low-pressure compressor outlet	MPa
T_{21}	Total temperature at low-pressure compressor outlet	K
P_3	Total pressure at high-pressure compressor outlet	MPa
T_3	Total temperature at high-pressure compressor outlet	K
P_5	Total pressure at high-pressure turbine outlet	MPa
P_{55}	Total pressure at low-pressure turbine outlet	MPa
T_{55}	Total temperature at low-pressure turbine outlet	K
Thrust	Thrust	kN
Pr_{221}	Pressure ratio of low-pressure compressor	
Pr_{253}	Pressure ratio of high-pressure compressor	
Pr_{45}	Pressure ratio of high-pressure turbine	
Pr_{555}	Pressure ratio of low-pressure turbine	

Table 2. Fault Settings of Aero-Engine Gas-Path Components.

Fault Type	Health Parameter	Relative Change from Nominal Value (%)
Low-Pressure Compressor Fault	Efficiency coefficient of low-pressure compressor	−1.05%
	Flow coefficient of low-pressure compressor	−2.04%
High-Pressure Compressor Fault	Efficiency coefficient of high-pressure compressor	−2.94%
	Flow coefficient of high-pressure compressor	−3.91%
High-Pressure Turbine Fault	Efficiency coefficient of high-pressure turbine	−2.63%
	Flow coefficient of high-pressure turbine	+1.76%
Low-Pressure Turbine Fault	Efficiency coefficient of low-pressure turbine	−1.00%
	Flow coefficient of low-pressure turbine	+0.40%

Considering the difficulty of obtaining real fault data, fault data are generated in this study using a nonlinear component-level aerothermodynamic model of a certain military turbofan engine. The simulated gas-path measurements are generated through the coupled response of the component-level engine model rather than by independently perturbing individual measured variables. In the model, the major gas-path components are constrained by flow continuity, spool power balance, and thermodynamic matching relationships. Therefore, perturbations introduced to component health parameters propagate through the nonlinear engine model and produce corresponding changes in measurable quantities such as rotational speed, pressure, and temperature.

Engine performance degradation and fault conditions are simulated by modifying the prescribed health parameters of the corresponding gas-path components, rather than by directly modifying the measured gas-path variables. The resulting measurable gas-path parameters are subsequently obtained from the component-level engine model under the specified component health state and operating condition. Consequently, a change in the health state of one component may cause simultaneous changes in multiple measured variables because of the inherent coupling among the gas-path components. Under different degradation levels and operating conditions, single and compound faults are collected for four components: the low-pressure compressor, high-pressure compressor, high-pressure

turbine, and low-pressure turbine. The fault simulation settings of engine components are shown in Table 3. In Table 3, "F" indicates that the corresponding component is faulty under a given mode, whereas "–" indicates that the corresponding component is normal. There are nine modes in total, including the normal state. Mode 9 represents the normal engine condition; Modes 1–4 correspond to single-component faults; and Modes 5–8 correspond to compound faults.

Table 3. Aero-Engine Gas-Path Fault Mode Settings.

Component	Fault Modes								
	1	**2**	**3**	**4**	**5**	**6**	**7**	**8**	**9**
LPC	F	-	-	-	F	-	F	F	-
HPC	-	F	-	-	F	-	F	-	-
HPT	-	-	F	-	-	F	F	F	-
LPT	-	-	-	F	-	F	-	F	-

This study focuses on aero-engine gas-path fault diagnosis under variable operating conditions. All datasets considered in this study are generated from the same underlying aero-engine configuration and the same component-level aero-thermodynamic model. Different operating conditions are established by specifying different combinations of flight altitude H and Mach number Ma, which determine the external flight boundary conditions of the engine. It should be emphasized that altitude and Mach number are not treated as the only variables describing the internal engine state. For each operating condition, the corresponding gas-path operating state is obtained from the engine model, and variations in the external flight condition are consequently reflected in changes in the internal gas-path parameters, including mass-flow-related quantities, spool rotational speeds, pressures, temperatures, pressure ratios, fuel flow, and thrust. Therefore, the gas-path parameters under different operating conditions are not artificially kept unchanged when H and Ma are varied. Four representative operating conditions are considered in this study, as summarized in Table 4. The specific details of the dataset are summarized in Table 5.

Table 4. Operating-Condition Parameters and Dataset Settings of the Aero-Engine Gas-Path Data.

Condition	Altitude	Mach Number	Normal Data Size	Fault Data Size
A	$H = 5.5$ km	$Ma = 0.8$	294	1381
B	$H = 6.5$ km	$Ma = 0.75$	489	1865
C	$H = 7.5$ km	$Ma = 0.75$	734	5517
D	$H = 9.5$ km	$Ma = 0.8$	695	5238

Table 5. Class-Wise Sample Distribution of Diagnostic Modes under Different Operating Conditions.

Condition	Diagnostic Modes								
	1	**2**	**3**	**4**	**5**	**6**	**7**	**8**	**9**
A	168	177	158	185	169	161	179	184	294
B	219	242	231	241	222	234	237	239	489
C	638	731	688	708	655	702	704	691	734
D	595	711	669	675	610	665	688	625	695

The four datasets A–D therefore represent different operating conditions of the same aero-engine model rather than data obtained from four different engines. The altitude–Mach-number pair in Table 4 specifies the external operating condition, whereas

the corresponding measured gas-path variables characterize the resulting internal engine state. Consequently, differences among datasets A–D include not only the changes in altitude and Mach number themselves but also the associated variations in the gas-path responses induced by the change in operating condition.

Four aero-engine gas-path datasets corresponding to different operating conditions are constructed in this study, based on which 12 transfer tasks are designed: A → B, A → C, A → D, B → A, B → C, B → D, C → A, C → B, C → D, D → A, D → B, and D → C. For each unsupervised transfer task, 80% of the labeled source-domain data and 60% of the unlabeled target-domain data are used for training. The remaining 20% of the source-domain data are used for validation, while the remaining 40% of the target-domain data are used for testing.

4.1.2. Model Parameter Setting and Evaluation Indicator

The detailed parameter settings of TG-RADAN are presented in Table 6.

Table 6. TG-RADAN Model Parameters and Training Settings.

Component	Configuration/Parameters
Input	Source domain data: arbitrary operating condition; Target domain data: another operating condition; Feature dimension: 15; Number of classes: 9
Feature Reweighting Module	TI-based feature reweighting; TI constructed via Fisher score and domain discrepancy; $\alpha = 0.6$, $\beta = 0.4$; gating weight range: 0.5–1.8
Feature Extractor	Residual-attention operating-condition-aware encoder; gas-path input dimension: 15; input projection: 15 → 128; two residual blocks; hidden dimension: 128; output feature dimension: 64; dropout: 0.2
Attention Module	Feature attention mechanism; reduction ratio: 4; attention weights generated via two fully connected layers and Sigmoid activation
Domain-Specific Normalization	DSBN with separate normalization statistics and affine parameters for source and target operating-condition domains; remaining encoder parameters are shared across domains
Domain Adaptation Mechanism	Adversarial domain adaptation framework; CDAN uses joint feature–prediction interaction for conditional alignment
Total Loss Function	Composed of classification loss, adversarial loss, prototype alignment loss, entropy minimization loss, and gating regularization term; $\lambda_{adv} = 1.0$, $\lambda_{proto} = 0.5$, $\lambda_{ent} = 0.05$
Optimizer & Training Settings	Adam optimizer; learning rate: 0.001; weight decay: 1×10^{-4}; batch size: 128; epochs: 70; random seed: 42
Output	9-class fault classification results

In this study, classification accuracy is adopted as the primary evaluation metric. For each target-domain test sample, the fault category corresponding to the maximum classifier output probability is taken as the predicted class. A test sample is considered correctly classified when its predicted fault category is identical to its ground-truth fault label. The classification accuracy is defined as:

$$Accuracy = \frac{N_{correct}}{N_{total}} \times 100\%, \tag{29}$$

where $N_{correct}$ denotes the number of correctly classified samples in the test set, and N_{total} denotes the total number of test samples. The target-domain ground-truth labels are

used only for final performance evaluation and are not involved in model training or domain adaptation.

4.2. Experimental Results

In this section, the diagnostic performance of TG-RADAN is comprehensively assessed through comparative experiments, ablation studies, analysis of the transferability-guided gating mechanism, and parameter sensitivity experiments. The comparative experiments are presented first.

4.2.1. Comparison with Representative Baseline Methods

To validate the superiority of the proposed model in fault diagnosis under variable operating conditions, it is compared with several representative methods, including multilayer perceptron (MLP), transfer component analysis (TCA), joint distribution adaptation (JDA), conditional domain adversarial network (CDAN), and domain-adversarial neural network (DANN) [34]. For a fair comparison, all methods are evaluated under the same data partitioning and preprocessing protocols. For each transfer task, the normalization statistics are estimated only from the source-domain training data and the unlabeled target-domain training data. The target-domain test data are transformed using these fixed statistics and are not used for training, hyperparameter tuning, or model selection.

For MLP, TCA, and JDA, the standardized raw gas-path features are used as inputs. MLP serves as a source-only supervised baseline, which is trained using only labeled source-domain data and directly evaluated on the target domain. For TCA and JDA, kernel-based cross-domain feature alignment is performed. The transfer subspace dimension, regularization parameter, and kernel function are set to 30, 1.0, and radial basis function (RBF), respectively. In addition, JDA iteratively aligns both marginal and conditional distributions, with the maximum number of iterations set to 10.

For the deep domain adaptation baselines, DANN and CDAN adopt a conventional two-layer multilayer perceptron (MLP) feature extractor, with a hidden dimension of 128 and an output feature dimension of 64. This configuration is used to represent standard adversarial domain adaptation baselines. The residual-attention encoder, DSBN, TI-guided gating, prototype alignment, and entropy minimization are not included in these baseline methods. The feature encoder consists of two fully connected layers, with a hidden dimension of 128 and an output feature dimension of 64. The ReLU activation function is used, and dropout with a rate of 0.2 is introduced to alleviate overfitting. The classifier contains nine output classes. During training, both DANN and CDAN are optimized using the Adam optimizer with a learning rate of 0.001, a batch size of 128, and 70 training epochs.

To reduce the influence of randomness, each experiment is repeated ten times, and the mean and standard deviation are reported as the final results. The fault diagnosis results of the proposed model and the comparison methods under different operating conditions are presented in Table 7.

As shown in Table 7, the proposed model demonstrates superior performance in aero-engine gas-path fault diagnosis under variable operating conditions. The conventional supervised learning method MLP performs the worst, achieving average accuracies of only 31.82% and 31.71% on six transfer tasks with A and B as source domains and six tasks with C and D as source domains, respectively. This indicates that significant distribution discrepancies exist between source and target domains under varying operating conditions, making models trained solely on source-domain data difficult to directly generalize to the target domain.

Compared with MLP, traditional transfer learning methods such as TCA and JDA can partially alleviate the domain shift problem. Specifically, TCA improves the average

accuracy to 53.59% and 53.39%, while JDA further increases it to 55.50% and 55.19%, respectively. These results indicate that jointly aligning marginal and conditional distributions is more effective than purely subspace-based transfer. However, the representation capability of these shallow methods remains limited when dealing with complex nonlinear operating-condition variations.

Table 7. Classification Accuracy of Different Methods on 12 Cross-Condition Transfer Tasks.

Method	**Accuracy/%**						**Average Accuracy**
	A → B	**A → C**	**A → D**	**B → A**	**B → C**	**B → D**	
MLP	40.02 ± 3.19	30.27 ± 3.32	22.51 ± 3.65	34.09 ± 3.41	38.63 ± 3.44	25.41 ± 3.69	31.82
TCA	56.73 ± 2.13	53.37 ± 2.99	50.42 ± 2.76	54.43 ± 2.53	55.21 ± 2.48	51.39 ± 3.05	53.59
JDA	58.26 ± 2.86	54.64 ± 2.56	51.77 ± 2.08	56.66 ± 2.07	58.02 ± 2.33	53.62 ± 2.76	55.50
DANN	81.37 ± 2.58	76.14 ± 2.73	73.36 ± 2.75	80.93 ± 2.16	79.31 ± 2.66	75.21 ± 2.78	77.72
CDAN	85.40 ± 2.30	81.25 ± 2.57	79.48 ± 2.13	84.17 ± 2.32	83.69 ± 2.43	80.92 ± 1.97	82.49
TG-RADAN	96.30 ± 0.60	94.07 ± 0.57	92.14 ± 1.02	96.03 ± 0.90	94.19 ± 1.01	93.85 ± 0.62	94.43
Method	Accuracy/%						Average Accuracy
	C → A	C → B	C → D	D → A	D → B	D → C	
MLP	30.31 ± 3.21	40.18 ± 3.49	35.39 ± 2.00	23.95 ± 3.43	24.96 ± 3.21	35.45 ± 3.44	31.71
TCA	52.11 ± 2.87	55.06 ± 2.13	56.11 ± 2.35	50.02 ± 2.63	51.33 ± 2.41	55.73 ± 2.52	53.39
JDA	54.22 ± 2.65	57.37 ± 2.61	58.31 ± 2.56	50.93 ± 2.15	52.37 ± 2.58	57.96 ± 2.47	55.19
DANN	76.06 ± 2.12	77.43 ± 2.44	81.23 ± 2.62	73.09 ± 2.83	75.61 ± 2.78	81.54 ± 2.75	77.49
CDAN	81.09 ± 2.11	81.01 ± 2.58	84.37 ± 1.98	78.41 ± 3.21	80.22 ± 2.49	83.91 ± 2.36	81.50
TG-RADAN	93.86 ± 0.53	94.17 ± 0.24	96.42 ± 0.64	92.79 ± 1.33	93.88 ± 1.04	95.31 ± 0.53	94.41

Deep domain adaptation methods, including DANN and CDAN, achieve significantly better transfer performance. DANN substantially outperforms TCA and JDA, while CDAN further improves the average accuracy by 4.77% and 4.01% compared with DANN, respectively, demonstrating that incorporating class-conditional information enables more effective cross-domain feature alignment and class discrimination.

Notably, the proposed method achieves the best performance across all 12 transfer tasks. Compared with CDAN, it improves the average accuracy by 11.94% and 12.91%, respectively, while also achieving lower standard deviations, indicating superior stability across repeated experiments.

4.2.2. Component-Wise Ablation Study

In this study, the term "ablation study" is used in the machine-learning sense, referring to controlled experiments in which individual model components are removed, added, or replaced while the remaining experimental settings are kept unchanged, so that the contribution of each component can be quantitatively evaluated.

To verify the contributions of each module in TG-RADAN for unsupervised cross-condition aero-engine gas-path fault diagnosis, and to further demonstrate that the performance improvement does not stem from a single component but from their joint collaboration, ablation experiments are conducted under the same data partitioning strategy, training protocol, and parameter settings. The ablation study focuses on the following three aspects: (1) whether each module in TG-RADAN contributes positively to cross-condition transfer performance; (2) whether the Transferability Index (TI) and its guided learnable gating mechanism can effectively identify and enhance transferable features; and (3) whether DSBN, prototype alignment, and entropy minimization provide complementary benefits in terms of statistical distribution adaptation and target-domain structural stability.

To systematically evaluate the contributions of the main components, the following ablation variants are constructed:

(1) B0: the baseline model consisting of a residual-attention encoder and a source-domain supervised classifier, without any domain adaptation mechanism;

(2) B1: B0 augmented with the conditional domain adversarial alignment (CDAN) module;

(3) B2: B1 further equipped with domain-specific batch normalization (DSBN) to mitigate statistical discrepancies between the source and target domains;

(4) B3: B2 plus prototype alignment;

(5) B4: B2 plus entropy minimization;

(6) B5: B2 combined with both prototype alignment and entropy minimization;

(7) B6: B5 further incorporating static feature weighting based on the Transferability Index;

(8) B7: the complete model, which replaces static weighting with TI-guided learnable gating and introduces a gating regularization term.

To reduce the influence of randomness, each cross-condition transfer task is repeated ten times, and the final results are reported as the average performance. The diagnostic results are summarized in Table 8.

Table 8. Classification Accuracy of Component-Wise Ablation Variants of TG-RADAN.

Ablated Model	**Accuracy/%**						**Average Accuracy**
	A → B	**A → C**	**A → D**	**B → A**	**B → C**	**B → D**	
B0	50.25 ± 3.24	41.36 ± 3.51	40.59 ± 3.14	48.37 ± 3.41	51.42 ± 3.23	41.65 ± 3.54	45.61
B1	90.16 ± 2.68	85.59 ± 2.66	83.47 ± 2.53	89.85 ± 2.61	88.76 ± 2.62	84.55 ± 2.57	87.06
B2	91.79 ± 2.34	87.61 ± 2.33	86.78 ± 2.28	91.43 ± 2.26	90.11 ± 2.31	87.38 ± 2.32	89.18
B3	92.69 ± 2.21	90.32 ± 2.27	88.51 ± 2.35	92.02 ± 2.22	90.59 ± 2.16	88.27 ± 2.11	90.40
B4	92.57 ± 2.26	91.25 ± 2.23	89.56 ± 2.16	92.27 ± 2.35	90.45 ± 2.33	88.26 ± 2.26	90.73
B5	93.42 ± 1.56	91.83 ± 1.43	90.15 ± 1.62	92.95 ± 1.34	91.47 ± 1.42	90.61 ± 1.45	91.74
B6	94.98 ± 1.32	93.09 ± 1.44	91.27 ± 1.14	94.52 ± 1.43	92.75 ± 1.05	92.11 ± 1.16	93.12
B7	96.30 ± 0.60	94.07 ± 0.57	92.14 ± 1.02	96.03 ± 0.90	94.19 ± 1.01	93.85 ± 0.62	94.43
Ablated Model	Accuracy/%						Average Accuracy
	C → A	C → B	C → D	D → A	D → B	D → C	
B0	40.73 ± 3.16	50.91 ± 3.25	47.28 ± 3.16	41.04 ± 3.44	42.58 ± 3.21	48.55 ± 3.47	45.18
B1	85.44 ± 2.54	85.39 ± 2.53	89.72 ± 2.63	83.70 ± 2.67	85.06 ± 2.46	88.46 ± 2.54	86.30
B2	88.50 ± 2.43	87.44 ± 2.45	90.94 ± 2.31	86.53 ± 2.31	87.27 ± 2.26	89.31 ± 2.28	88.33
B3	89.05 ± 2.43	88.97 ± 2.34	92.11 ± 2.11	88.15 ± 2.25	89.60 ± 2.27	90.84 ± 2.12	89.79
B4	89.27 ± 2.24	89.16 ± 2.21	92.31 ± 2.32	88.40 ± 2.41	90.19 ± 2.16	90.97 ± 2.17	90.05
B5	90.91 ± 1.61	90.52 ± 1.43	93.23 ± 1.54	89.79 ± 1.64	90.84 ± 1.68	91.98 ± 1.32	91.21
B6	93.25 ± 1.24	92.71 ± 1.31	94.33 ± 1.42	91.32 ± 1.11	92.46 ± 1.08	94.02 ± 1.21	93.02
B7	93.86 ± 0.53	94.17 ± 0.24	96.42 ± 0.64	92.79 ± 1.33	93.88 ± 1.04	95.31 ± 0.53	94.41

As shown in Table 8, among all ablation variants, B7 achieves the best performance across all 12 cross-condition transfer tasks. Specifically, the baseline model B0 achieves relatively low average accuracies of 45.61% and 45.18% on the six tasks with A and B as source domains and the six tasks with C and D as source domains, respectively. After introducing the domain adaptation module CDAN, B1 significantly improves the performance to 87.06% and 86.30%, demonstrating that class-conditional alignment can effectively alleviate domain shift.

Further improvements are observed when DSBN is incorporated. B2 outperforms B1 by 2.12% and 2.03%, respectively, indicating that separately modeling the statistical characteristics of the source and target domains helps reduce the interference caused by operating-condition variations in latent representations. Subsequently, both B3 with prototype alignment and B4 with entropy minimization yield additional gains over B2. When combining both components in B5, the average accuracy reaches 91.74% and 91.21%, respectively, suggesting that adversarial alignment alone is insufficient to stabilize the

target-domain class structure. Instead, both clustering constraints and confidence regularization are necessary to suppress confusion between similar and compound fault modes.

Building upon this, introducing static TI-based feature weighting in B6 further improves performance, indicating that gas-path features exhibit non-uniform transferability in cross-condition aero-engine scenarios. Prioritizing features that are both stable across operating conditions and highly fault-discriminative can significantly enhance diagnostic performance. Finally, B7 with TI-guided learnable gating achieves the highest accuracy of 94.43% and 94.41%, demonstrating that, compared with static weighting, combining transferability priors with dynamic feature gating is more effective in handling heterogeneous feature shifts under varying operating conditions.

To further illustrate the classification performance of each ablation model across fault categories, confusion matrices are introduced. The confusion matrices of B2, B5, B6, and B7 under the A → B transfer task are shown in Figure 7.

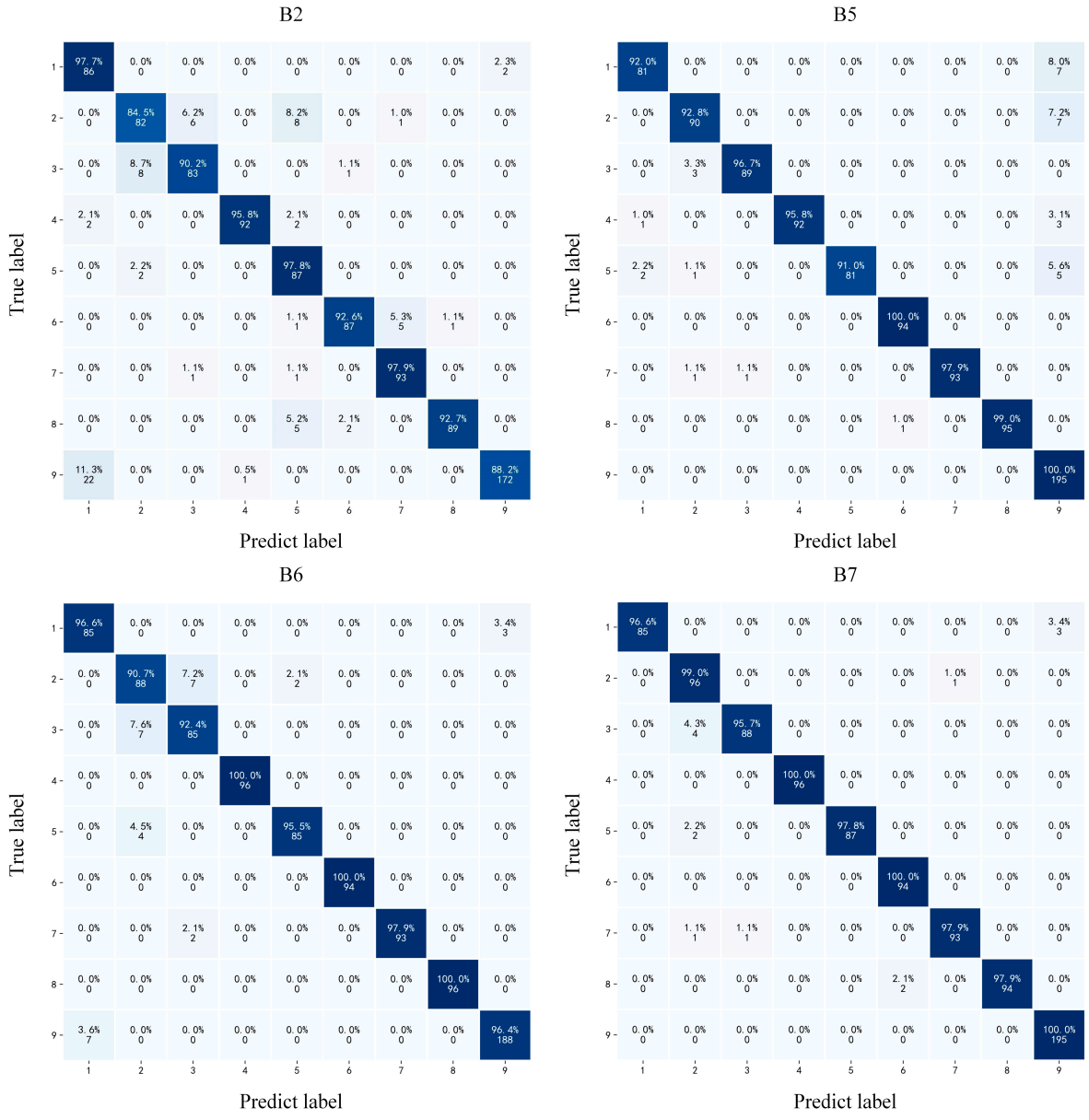


Figure 7. Confusion Matrices of Different Ablation Models Under the A → B Transfer Task.

As shown in Figure 7, although B2 is able to achieve relatively satisfactory cross-condition fault diagnosis performance, evident misclassification can still be observed among

class 2 and class 3, class 1 and class 9, as well as class 6 and class 7. After incorporating prototype alignment and entropy minimization, B5 significantly alleviates the above inter-class confusion.

Compared with B5, both B6 and B7 exhibit a more concentrated diagonal distribution in the confusion matrices, with B7 achieving the best overall performance. These results indicate that, in cross-condition aero-engine gas-path fault diagnosis, introducing static TI-based weighting can preliminarily suppress negative transfer caused by operating-condition-sensitive features. Furthermore, the TI-guided learnable gating mechanism can further highlight transfer-stable and fault-discriminative gas-path features, thereby improving the classification accuracy of each fault category.

4.2.3. Parameter Sensitivity Analysis

To further evaluate the robustness of TG-RADAN in unsupervised cross-condition aero-engine gas-path fault diagnosis, a sensitivity analysis is conducted on the key model hyperparameters. Based on the overall objective in Equation (28), particular attention is given to the effects of the adversarial loss weight λ_{adv}, prototype alignment loss weight λ_{proto}, entropy minimization loss weight λ_{ent}, and gating regularization weight λ_{gate} on diagnostic performance. A control-variable strategy is adopted, in which only one parameter is varied at a time, while all remaining parameters are fixed at their default values listed in Table 5. Figure 8 illustrates the influence of these weighting coefficients on model performance for the A $\rightarrow$ B transfer task.

As shown in Figure 8a, λ_{adv} balances source-domain fault discriminability against the strength of cross-condition domain alignment. When λ_{adv} is small, the model relies primarily on source-domain supervised classification, and the shifts in gas-path parameters caused by variations in altitude and Mach number cannot be adequately corrected in the target domain, resulting in relatively low diagnostic accuracy. As λ_{adv} increases to 1.0, the distribution discrepancy between the source and target domains is effectively reduced, and the highest accuracy is achieved. However, a further increase in λ_{adv} imposes an excessively strong adversarial constraint, which may weaken the class-discriminative structure of the source domain and induce class confusion, thereby degrading diagnostic performance. These results indicate that domain invariance and fault discriminability must be appropriately balanced in cross-condition aero-engine gas-path fault diagnosis.

Figure 8b,c present the effects of λ_{proto} and λ_{ent}, respectively, on target-domain structure preservation. As λ_{proto} increases from 0.0 to 0.5, the prototype alignment constraint progressively strengthens cross-domain class consistency, leading to improved accuracy. When λ_{proto} exceeds 0.5, however, the performance becomes saturated and even slightly declines, indicating that an overly strong prototype constraint may amplify pseudo-label errors. Similarly, increasing λ_{ent} from 0.0 to 0.05 encourages more confident target-domain predictions and improves diagnostic accuracy. Further increasing λ_{ent}, however, results in performance degradation, suggesting that excessive confidence regularization may prematurely assign incorrect labels to insufficiently aligned samples. These observations demonstrate that λ_{proto} and λ_{ent} achieve the best performance within moderate ranges. For gas-path fault diagnosis problems characterized by strong inter-class similarity and pronounced confusion between compound and single faults, appropriately designed structural constraints are required to jointly enhance target-domain cluster quality and prediction stability.

Figure 8d analyzes the influence of λ_{gate} on model performance. The role of λ_{gate} is to regulate the consistency between the learnable gating weights and the TI-based transferability prior. When λ_{gate} is relatively small, the gating weights are more susceptible to the joint effects of adversarial gradients and pseudo-label noise, which may lead to deviations in the learned weights and an undesirable enhancement of condition-sensitive features,

thereby reducing the stability and reliability of cross-condition transfer learning. As λ_{gate} gradually increases to 0.06, the gating mechanism achieves a more appropriate balance between the TI prior and the task-driven learning objective, yielding the highest diagnostic accuracy. A further increase in λ_{gate}, however, over-constrains the gating weights toward the TI prior and limits their flexibility to adapt dynamically to fault-discrimination and domain-alignment requirements, resulting in degraded performance. These findings indicate that the TI-guided gating mechanism does not simply rely on static prior information; rather, it achieves effective feature reweighting through coordinated optimization between prior regularization and learnable task-driven adaptation.

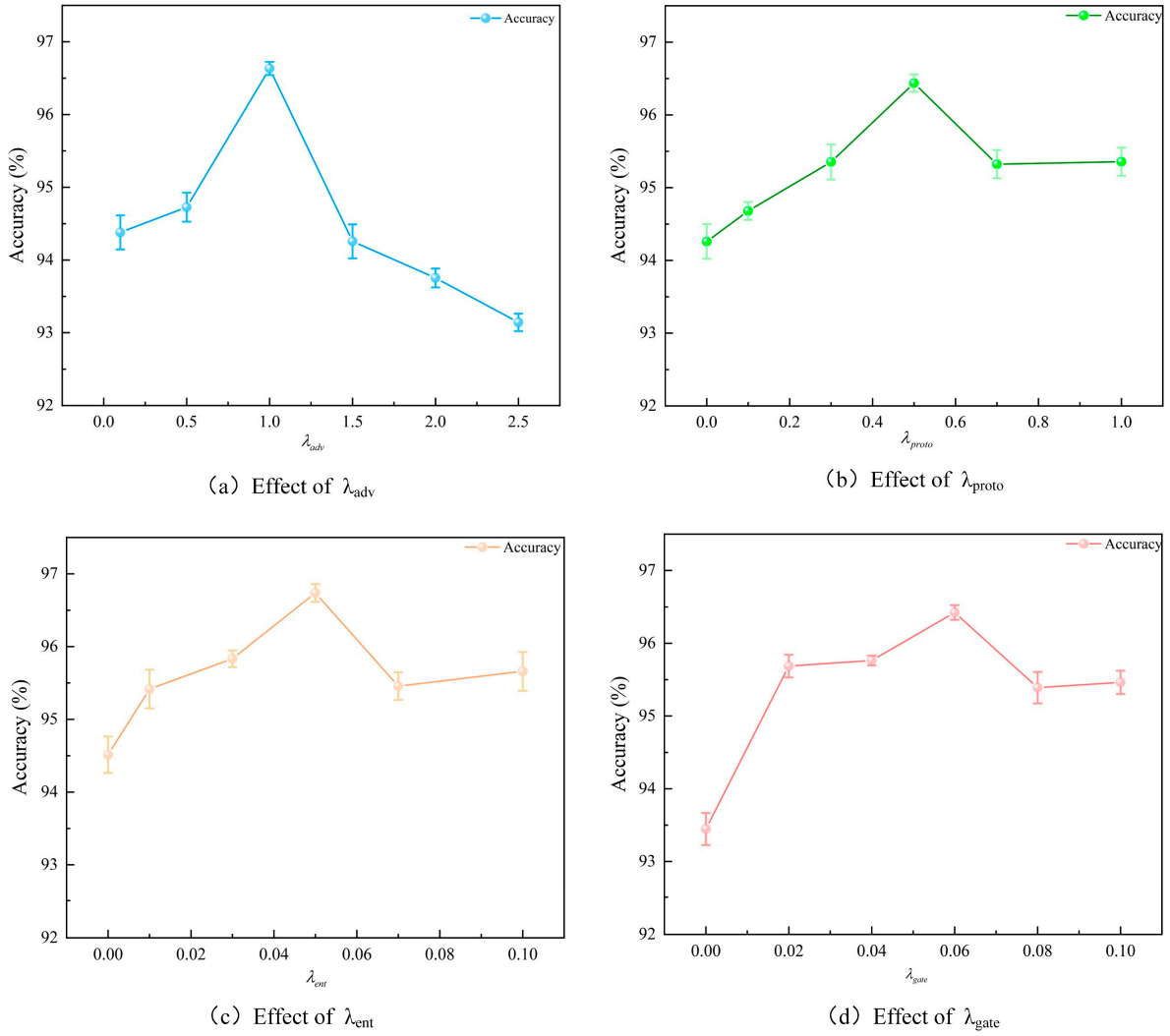


Figure 8. Sensitivity Analysis of Key Loss Weights in TG-RADAN.

4.3. Feature Visualization and Interpretability Analysis of the Gating Mechanism

To further investigate the role and underlying mechanism of TG-RADAN in cross-condition gas-path fault diagnosis of aero-engines, this study conducts analysis from two perspectives: feature distribution characteristics and input-weight allocation patterns. Domain A is selected as the source domain, and Domain B as the target domain. The T-SNE visualization of the original feature distributions in the source and target domains is presented in Figure 9.

Figure 9 shows that the original features exhibit a certain degree of clustering tendency with respect to fault categories. However, a pronounced distribution shift exists between the source and target domains. In particular, intra-class compactness across the two domains

is insufficient, and the decision boundaries of several fault categories remain ambiguous, leading to noticeable inter-class confusion. This phenomenon indicates that the raw gas-path parameters are jointly influenced by both fault states and operating conditions, making direct cross-condition fault diagnosis challenging.

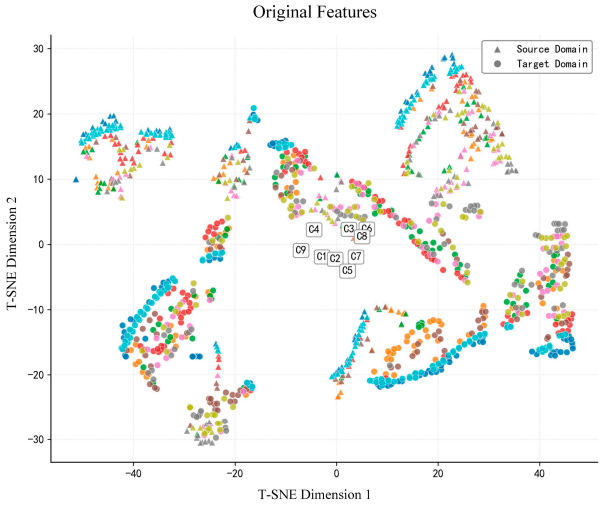


Figure 9. T-SNE Visualization of Original Source and Target Domain Features in the A → B Transfer Task.

To further validate the effectiveness of the proposed components, ablation models B0, B2, B5, and B7 are selected for comparison. The corresponding T-SNE visualizations of feature distributions for each ablated variant are presented in Figure 10.

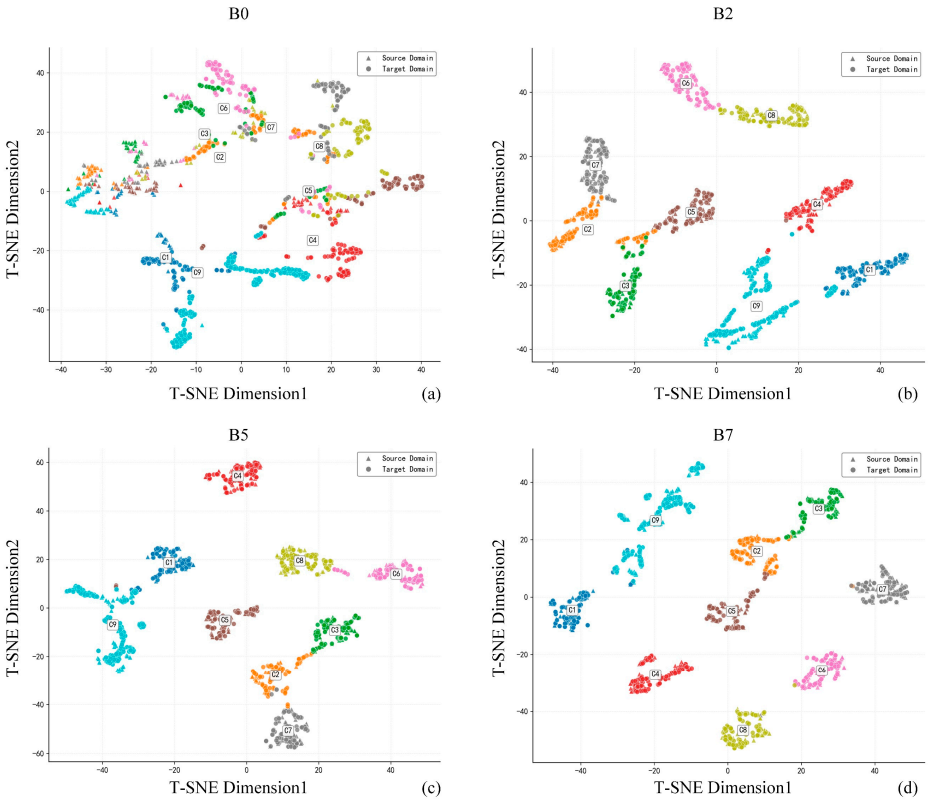


Figure 10. T-SNE Visualization of Deep Features of Different Models in the A → B Transfer Task.

From Figure 10, it can be observed that the baseline model B0, compared with the original gas-path feature distribution, is able to form preliminary decision boundaries

between different fault categories. However, a clear distribution discrepancy between the source and target domains still exists, and severe inter-class confusion remains for several categories. This indicates that relying solely on source-domain supervised learning is insufficient for cross-condition fault diagnosis.

After incorporating CDAN and DSBN, model B2 exhibits a reduced domain discrepancy, and the class boundaries become more distinct. Building upon this, B5 further integrates prototype alignment and entropy minimization, leading to improved intra-class compactness and enhanced inter-class separability. Finally, the complete model B7 achieves the most compact feature clusters, with the highest degree of overlap between source and target samples within the same class, while simultaneously exhibiting the clearest separation among different fault categories. These results demonstrate that TG-RADAN can effectively achieve both cross-domain distribution alignment and preservation of discriminative fault structures.

To further investigate the role of the transferability-guided gating mechanism in TG-RADAN, the prior Transferability Index (TI) of 15 gas-path features in the A → B transfer task is compared with the learned gating weights. The corresponding results are shown in Figure 11.

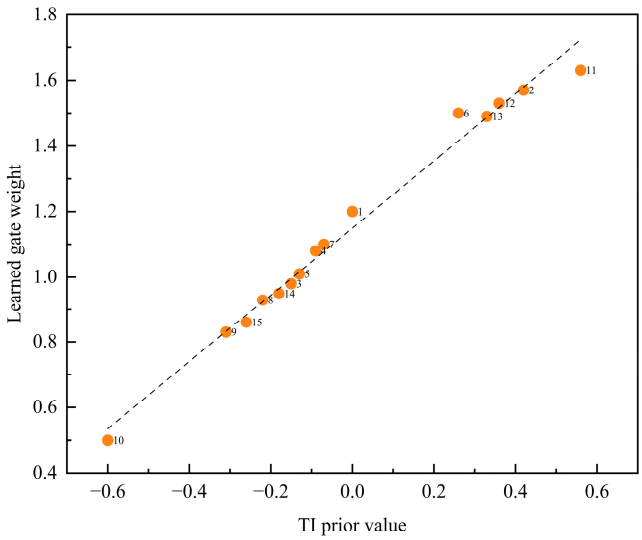


Figure 11. Comparison Between TI Prior Values and Learnable Gating Weights in the A → B Transfer Task.

Figure 11 shows that the TI prior values and the learned gating weights exhibit an overall strong positive correlation. This indicates that the gating mechanism is generally consistent with the TI-based assessment of feature transferability, assigning higher weights to features with stronger transferability while suppressing those with weaker transferability. Accordingly, the TI not only provides a static evaluation of feature transferability but also effectively guides the optimization direction of the learnable gating module.

A more detailed analysis reveals that features 2, 6, 11, 12, and 13, corresponding to the high-pressure spool rotational speed, high-pressure-compressor outlet total pressure, thrust, low-pressure-compressor pressure ratio, and high-pressure-compressor pressure ratio, respectively, receive relatively high gating weights. These parameters are closely associated with the overall engine operating capability, compressor pressurization performance, and rotor dynamic state. They can stably reflect efficiency degradation and flow variation in gas-path components and thus possess high transfer value in cross-condition fault diagnosis.

In contrast, features 8, 9, 10, 14, and 15, corresponding to the high-pressure-turbine outlet total pressure, low-pressure-turbine outlet total pressure, low-pressure-turbine outlet

total temperature, high-pressure-turbine pressure ratio, and low-pressure-turbine pressure ratio, respectively, are assigned relatively low gating weights. These features are more sensitive to operating-condition variations in the considered transfer task. If directly involved in global alignment, they may introduce condition-specific information and potentially lead to negative transfer. By down-weighting these features, the model effectively mitigates their interference in subsequent learning.

Notably, the final learned gating weights do not exactly replicate the TI prior. For instance, feature 1 exhibits a moderate TI value but is assigned a relatively higher learned weight. This suggests that the proposed gating mechanism does not merely follow the TI prior in a rigid manner, but instead performs adaptive adjustment under the joint constraints of transferability, classification loss, adversarial alignment, and structural preservation objectives.

5. Conclusions

This study proposed a Transferability-Guided Residual Attention Domain Adaptation Network (TG-RADAN) for unsupervised cross-condition aero-engine gas-path fault diagnosis. The proposed framework integrates TI-guided input feature reweighting, residual-attention-based condition-aware representation learning, domain-specific batch normalization, conditional adversarial alignment, prototype alignment, and target entropy minimization into a unified optimization framework.

The TI-guided learnable gating mechanism evaluates the transfer potential of gas-path parameters by jointly considering source-domain discriminability and cross-condition distribution stability. This mechanism enables the model to emphasize transferable fault-related features while suppressing operating-condition-sensitive variables. The residual-attention encoder with DSBN further improves the stability of deep feature extraction by preserving discriminative representations and reducing hidden statistical discrepancies between source and target domains. In addition, the combination of conditional adversarial alignment, prototype alignment, and entropy minimization enhances target-domain class compactness and prediction confidence.

Experimental results on 12 cross-condition transfer tasks show that TG-RADAN achieves average accuracies of 94.43% and 94.41% on the two groups of transfer tasks, respectively. Compared with the conventional CDAN baseline, the proposed model improves the average accuracy by 11.94% and 12.91%, respectively. The ablation study further demonstrates that TI-guided feature gating contributes 2.69% and 3.20% average accuracy improvements over the model without this module.

From a physical and engineering perspective, the diagnostic outputs of TG-RADAN are associated with the health states of gas-path components reflected by measurable engine parameters, including spool rotational speeds, pressures, temperatures, fuel flow, thrust, and component pressure ratios. In a real gas turbine engine, deterioration of component efficiency and flow-capacity characteristics propagates through the coupled thermodynamic system and results in corresponding changes in these gas-path measurements. Therefore, the predicted fault states obtained by TG-RADAN can be interpreted as identifying component-health abnormalities from their cross-condition gas-path response patterns. In particular, by suppressing operating-condition-induced variations while preserving fault-discriminative information, the proposed framework provides potential engineering value for transferring diagnostic knowledge across flight conditions characterized by different altitudes and Mach numbers. Nevertheless, this physical relevance should currently be interpreted as mechanism-consistent engineering potential rather than direct validation on a real engine.

https://doi.org/10.3390/aerospace13090774

Despite this physical relevance and the strong performance demonstrated on the simulated aero-engine gas-path dataset, several limitations remain. The current study is based on component-level aerothermodynamic simulation data and does not yet account for real sensor noise, sensor bias, missing measurements, or complex degradation trajectories in practical engine operation or stochastic cross-component co-degradation dependencies that may arise during long-term engine operation. Future work will validate the proposed method using aero-engine test-bench or flight-monitoring data, investigate robustness under sensor uncertainty and weak-fault conditions, and extend the framework to multi-source and continuously varying operating-condition scenarios.

Author Contributions: Conceptualization, H.X.; methodology, H.X.; software, H.X.; validation, H.X.; formal analysis, H.X.; investigation, H.X. and K.C.; resources, K.C.; data curation, H.X.; writing—original draft preparation, H.X.; writing—review and editing, L.C.; visualization, H.X.; supervision, L.C.; project administration, K.C.; funding acquisition, K.C. All authors have read and agreed to the published version of the manuscript.

Funding: This research was supported by the Jiangxi Provincial Double-Thousand Talents Program (jxsq2018106057), funded by the Jiangxi Provincial Government.

Data Availability Statement: The data presented in this study are based on numerical simulations conducted in a controlled environment. No publicly archived datasets were generated or analyzed during this research. The simulation codes and intermediate results are not publicly available due to laboratory restrictions but can be obtained from the corresponding author upon reasonable request.

Conflicts of Interest: The authors declare no conflicts of interest.

References

1. Ahmad, S.H.; Kai, J.H.; Rabiu, B.I.; Hassan, S.M.H.U. Fault diagnosis of aircraft engine using an ANN-BiGRU based on perturbation strategy. *Aerosp. Sci. Technol.* **2026**, *168*, 111047. [CrossRef]
2. Qiu, S.; Cui, X.; Ping, Z.; Shan, N.; Li, Z.; Bao, X.; Xu, X. Deep learning techniques in intelligent fault diagnosis and prognosis for industrial systems: A review. *Sensors* **2023**, *23*, 1305. [CrossRef] [PubMed]
3. Cen, J.; Yang, Z.; Liu, X.; Xiong, J.; Chen, H. A review of data-driven machinery fault diagnosis using machine learning algorithms. *J. Vib. Eng. Technol.* **2022**, *10*, 2481–2507. [CrossRef]
4. Chorowski, J.; Wang, J.; Zurada, J.M. Review and performance comparison of SVM-and ELM-based classifiers. *Neurocomputing* **2014**, *128*, 507–516. [CrossRef]
5. Liu, X.; Chen, Y.; Xiong, L.; Wang, J.; Luo, C.; Zhang, L.; Wang, K. Intelligent fault diagnosis methods toward gas turbine: A review. *Chin. J. Aeronaut.* **2024**, *37*, 93–120. [CrossRef]
6. Liu, L.; Hao, C.; Xiong, L.; Lv, X. Physics-guided cross-domain adaptation: A hierarchical hybrid transformer framework with contrastive learning for robust fault diagnosis under variable working conditions. *Sci. Rep.* **2026**. *online ahead of print*. [CrossRef] [PubMed]
7. Chen, Z.; Zhang, W.; Zhao, W.; Yang, X.; Zhang, X.; Li, Y. Cross-condition fault diagnosis of chillers based on an ensemble approach with adaptive weight allocation. *Energy Build.* **2024**, *325*, 115007. [CrossRef]
8. Hu, J.; Li, W.; Wu, A.; Tian, Z. Novel joint transfer fine-grained metric network for cross-domain few-shot fault diagnosis. *Knowl.-Based Syst.* **2023**, *279*, 110958. [CrossRef]
9. Li, J.; Yu, Z.; Du, Z.; Zhu, L.; Shen, H.T. A comprehensive survey on source-free domain adaptation. *IEEE Trans. Pattern Anal. Mach. Intell.* **2024**, *46*, 5743–5762. [CrossRef] [PubMed]
10. Liu, M.; Mu, J.; Yu, Z.; Ruan, K.; Shu, B.; Yang, J. Adversarial learning and decomposition-based domain generalization for face anti-spoofing. *Pattern Recognit. Lett.* **2022**, *155*, 171–177. [CrossRef]
11. Han, T.; Liu, C.; Yang, W.; Jiang, D. Deep transfer network with joint distribution adaptation: A new intelligent fault diagnosis framework for industry application. *ISA Trans.* **2020**, *97*, 269–281. [CrossRef] [PubMed]
12. Shao, S.; McAleer, S.; Yan, R.; Baldi, P. Highly accurate machine fault diagnosis using deep transfer learning. *IEEE Trans. Ind. Inform.* **2018**, *15*, 2446–2455. [CrossRef]
13. Guo, L.; Lei, Y.; Xing, S.; Yan, T.; Li, N. Deep convolutional transfer learning network: A new method for intelligent fault diagnosis of machines with unlabeled data. *IEEE Trans. Ind. Electron.* **2019**, *66*, 7316–7325. [CrossRef]

14. Sun, C.; Ma, M.; Zhao, Z.; Tian, S.; Yan, R.; Chen, X. Deep transfer learning based on sparse autoencoder for remaining useful life prediction of tool in manufacturing. *IEEE Trans. Ind. Inform.* **2018**, *15*, 2416–2425. [CrossRef]
15. Qiao, H.; Wang, T.; Wang, P.; Zhang, L.; Xu, M. An adaptive weighted multiscale convolutional neural network for rotating machinery fault diagnosis under variable operating conditions. *IEEE Access* **2019**, *7*, 118954–118964. [CrossRef]
16. Jin, Z.; Liu, J.; Xu, M.; Miao, H.; Song, Z. An enhanced digital twin-driven fault detection and isolation method based on sensor series imaging mechanism for gas turbine engine. *Appl. Therm. Eng.* **2024**, *257*, 124308. [CrossRef]
17. Zhang, S.; Zhang, S.; Wang, B.; Habetler, T.G. Deep learning algorithms for bearing fault diagnostics—A comprehensive review. *IEEE Access* **2020**, *8*, 29857–29881. [CrossRef]
18. Sarwar, U.; Muhammad, M.; Mokhtar, A.A.; Khan, R.; Behrani, P.; Kaka, S. Hybrid intelligence for enhanced fault detection and diagnosis for industrial gas turbine engine. *Results Eng.* **2024**, *21*, 101841. [CrossRef]
19. Wang, B.; Xuan, Y. An integrated model for energy management of aero engines based on thermodynamic principle of variable mass systems. *Energy* **2023**, *276*, 127531. [CrossRef]
20. Sabzehali, M.; Alibeigi, M.; Aliabadi, S.K. Low-emission methane fueled dual-bypass turbofan engine optimization based on machine learning: Energy-economic-environmental (3E) analysis. *Clean. Eng. Technol.* **2025**, *26*, 100919. [CrossRef]
21. Rath, N.; Mishra, R.; Kushari, A. Aero engine health monitoring, diagnostics and prognostics for condition-based maintenance: An overview. *Int. J. Turbo Jet-Engines* **2023**, *40*, s279–s292. [CrossRef]
22. Volponi, A.J. Gas turbine engine health management: Past, present, and future trends. *J. Eng. Gas Turbines Power* **2014**, *136*, 051201. [CrossRef]
23. Wang, S.; Jiang, Y.; Guo, C.; Cui, R.; Xia, W. Transfer learning-based dual-branch multi-fidelity heterogeneous data fusion framework for aerodynamic performance prediction. *Aerosp. Sci. Technol.* **2026**, *168*, 110778. [CrossRef]
24. Shen, P.; Bi, F.; Bi, X.; Yang, X.; Tang, D.; Guo, M. A generative transfer learning method for extreme class imbalance problem and applied to piston aero-engine fault cross-domain diagnosis. *IEEE Trans. Reliab.* **2025**, *74*, 2434–2447. [CrossRef]
25. Fang, Y.; Yap, P.-T.; Lin, W.; Zhu, H.; Liu, M. Source-free unsupervised domain adaptation: A survey. *Neural Netw.* **2024**, *174*, 106230. [CrossRef] [PubMed]
26. Gu, Q.; Li, Z.; Han, J. Generalized fisher score for feature selection. In *Proceedings of the 27th Conference Uncertainty in Artificial Intelligence (UAI)*; AUAI Press: Arlington, VA, USA, 2011; pp. 266–273.
27. Liu, Q.; Huang, X. A new method of fault diagnosis for aeroengines with dispersedly clumped gas path parameters. *Aerosp. Sci. Technol.* **2024**, *148*, 109065. [CrossRef]
28. Hu, J.; Shen, L.; Sun, G. Squeeze-and-excitation networks. In Proceedings of the IEEE Conference on Computer Vision and Pattern Recognition, Salt Lake City, UT, USA, 18–23 June 2018; pp. 7132–7141.
29. Long, M.; Cao, Z.; Wang, J.; Jordan, M.I. Conditional adversarial domain adaptation. *Adv. Neural Inf. Process. Syst.* **2018**, *31*, 1647–1657.
30. Tang, H.; Chen, K.; Jia, K. Unsupervised domain adaptation via structurally regularized deep clustering. In Proceedings of the IEEE/CVF Conference on Computer Vision and Pattern Recognition, Seattle, WA, USA, 13–19 June 2020; pp. 8725–8735.
31. Wang, Z.; Wang, Y.; Wang, X.; Zhao, B.; Zhao, Y. Engine gas path component fault diagnosis based on a sparse deep stacking network. *Heliyon* **2023**, *9*, e19252. [CrossRef] [PubMed]
32. DeCastro, J.; Litt, J.; Frederick, D. A Modular Aero-Propulsion System Simulation of a Large Commercial Aircraft Engine. In Proceedings of the 44th AIAA/ASME/SAE/ASEE Joint Propulsion Conference & Exhibit, Hartford, CT, USA, 21–23 July 2008.
33. Lei, Y.; Li, N.; Guo, L.; Li, N.; Yan, T.; Lin, J. Machinery health prognostics: A systematic review from data acquisition to RUL prediction. *Mech. Syst. Signal Process.* **2018**, *104*, 799–834. [CrossRef]
34. HassanPour Zonoozi, M.; Seydi, V. A survey on adversarial domain adaptation. *Neural Process. Lett.* **2023**, *55*, 2429–2469. [CrossRef]

Disclaimer/Publisher's Note: The statements, opinions and data contained in all publications are solely those of the individual author(s) and contributor(s) and not of MDPI and/or the editor(s). MDPI and/or the editor(s) disclaim responsibility for any injury to people or property resulting from any ideas, methods, instructions or products referred to in the content.